

AD 727983

DASA-2699

DYNAMIC FRACTURE EXPERIMENTS USING
HIGH-ENERGY PULSED ELECTRON BEAMS

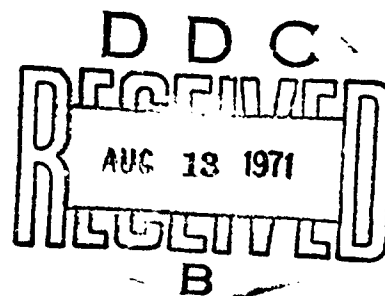
Tibor Stefansky and James H. Shea

July 1971

DEFENSE ATOMIC SUPPORT AGENCY
WASHINGTON, D. C. 20305

Approved for public release;
distribution unlimited.

Reproduced by
NATIONAL TECHNICAL
INFORMATION SERVICE
Springfield, Va. 22151



Preparing Agency
PHYSICS INTERNATIONAL COMPANY
2700 Merced Street
San Leandro, California 94577
Under Contract DASA 01-68-C-0138

UNCLASSIFIED

Security Classification

DOCUMENT CONTROL DATA - R&D

(Security classification of title, body of abstract and indexing annotation must be entered when the overall report is classified)

| | | | |
|--|--|--|-----------------------|
| 1. ORIGINATING ACTIVITY (Corporate author) Physics International Company 2700 Merced Street San Leandro, California 94577 | | 2a. REPORT SECURITY CLASSIFICATION Unclassified | |
| | | 2b. GROUP | |
| 3. REPORT TITLE Dynamic Fracture Experiments Using High-Energy Pulsed Electron Beams | | | |
| 4. DESCRIPTIVE NOTES (Type of report and inclusive dates) Final | | | |
| 5. AUTHOR(S) (Last name, first name, initial) Stefansky, Tibor and Shea, James H. | | | |
| 6. REPORT DATE July 1971 | | 7a. TOTAL NO. OF PAGES 107 | 7b. NO. OF REFS 14 |
| 8a. CONTRACT OR GRANT NO. DASA 01-68-C-0138 | | 9a. ORIGINATOR'S REPORT NUMBER(S) PIFR-108 | |
| b. PROJECT NO. NWER XAXA | | | |
| c. Task and Subtask AA 106 | | 9b. OTHER REPORT NO(S) (Any other numbers that may be assigned this report) DASA-2699 | |
| d. Work Unit 06 | | | |
| 10. AVAILABILITY/LIMITATION NOTICES Approved for public release; distribution unlimited. | | | |
| 11. SUPPLEMENTARY NOTES | | 12. SPONSORING MILITARY ACTIVITY Director Defense Atomic Support Agency Washington, D. C. 20305 | |

13. ABSTRACT

This report describes the results of an experimental effort in which high-energy pulsed electron beams were used to study dynamic fracture induced by rapid in-depth heating. The work was performed under the metals portion of the PREDIX* program; the materials studied were 6061-T6 aluminum, alpha titanium and OFHC copper. Spallation thresholds for these materials are presented in terms of the absorbed energy required to cause a specified amount of damage as a function of the tensile pulse duration. Differences in the loading paths resulting from plate impact on the one hand and rapid in-depth heating on the other hand are also described.

* Contract No. DASA 01-68-C-0138

UNCLASSIFIED
Security Classification

| 14 KEY WORDS | LINK A | | LINK B | | LINK C | |
|-----------------------|--------|----|--------|----|--------|----|
| | ROLE | WT | ROLE | WT | ROLE | WT |
| Fracture | | | | | | |
| Spallation | | | | | | |
| Pulsed electron beams | | | | | | |

INSTRUCTIONS

1. **ORIGINATING ACTIVITY:** Enter the name and address of the contractor, subcontractor, grantee, Department of Defense activity or other organization (*corporate author*) issuing the report.

2a. **REPORT SECURITY CLASSIFICATION:** Enter the overall security classification of the report. Indicate whether "Restricted Data" is included. Marking is to be in accordance with appropriate security regulations.

2b. **GROUP:** Automatic downgrading is specified in DoD Directive S200.10 and Armed Forces Industrial Manual. Enter the group number. Also, when applicable, show that optional markings have been used for Group 3 and Group 4 as authorized.

3. **REPORT TITLE:** Enter the complete report title in all capital letters. Titles in all cases should be unclassified. If a meaningful title cannot be selected without classification, show title classification in all capitals in parenthesis immediately following the title.

4. **DESCRIPTIVE NOTES:** If appropriate, enter the type of report, e.g., interim, progress, summary, annual, or final. Give the inclusive dates when a specific reporting period is covered.

5. **AUTHOR(S):** Enter the name(s) of author(s) as shown on or in the report. Enter last name, first name, middle initial. If military, show rank and branch of service. The name of the principal author is an absolute minimum requirement.

6. **REPORT DATE:** Enter the date of the report as day, month, year, or month, year. If more than one date appears on the report, use date of publication.

7a. **TOTAL NUMBER OF PAGES:** The total page count should follow normal pagination procedures, i.e., enter the number of pages containing information.

7b. **NUMBER OF REFERENCES:** Enter the total number of references cited in the report.

8a. **CONTRACT OR GRANT NUMBER:** If appropriate, enter the applicable number of the contract or grant under which the report was written.

8b, 8c, & 8d. **PROJECT NUMBER:** Enter the appropriate military department identification, such as project number, subproject number, system numbers, task number, etc.

9a. **ORIGINATOR'S REPORT NUMBER(S):** Enter the official report number by which the document will be identified and controlled by the originating activity. This number must be unique to this report.

9b. **OTHER REPORT NUMBER(S):** If the report has been assigned any other report numbers (either by the originator or by the sponsor), also enter this number(s).

10. **AVAILABILITY/LIMITATION NOTICES:** Enter any limitations on further dissemination of the report, other than those

imposed by security classification, using standard statements such as:

- (1) "Qualified requesters may obtain copies of this report from DDC."
- (2) "Foreign announcement and dissemination of this report by DDC is not authorized."
- (3) "U. S. Government agencies may obtain copies of this report directly from DDC. Other qualified DDC users shall request through _____."
- (4) "U. S. military agencies may obtain copies of this report directly from DDC. Other qualified users shall request through _____."
- (5) "All distribution of this report is controlled. Qualified DDC users shall request through _____."

If the report has been furnished to the Office of Technical Services, Department of Commerce, for sale to the public, indicate this fact and enter the price, if known.

11. **SUPPLEMENTARY NOTES:** Use for additional explanatory notes.

12. **SPONSORING MILITARY ACTIVITY:** Enter the name of the departmental project office or laboratory sponsoring (paying for) the research and development. Include address.

13. **ABSTRACT:** Enter an abstract giving a brief and factual summary of the document indicative of the report, even though it may also appear elsewhere in the body of the technical report. If additional space is required, a continuation sheet shall be attached.

It is highly desirable that the abstract of classified reports be unclassified. Each paragraph of the abstract shall end with an indication of the military security classification of the information in the paragraph, represented as (TS), (S), (C), or (U).

There is no limitation on the length of the abstract. However, the suggested length is from 150 to 225 words.

14. **KEY WORDS:** Key words are technically meaningful terms or short phrases that characterize a report and may be used as index entries for cataloging the report. Key words must be selected so that no security classification is required. Identifiers, such as equipment model designation, trade name, military project code name, geographic location, may be used as key words but will be followed by an indication of technical context. The assignment of links, roles, and weights is optional.

ILLUSTRATIONS

| <u>Figure</u> | <u>Page</u> |
|--|-------------|
| 3.1 Block Diagram of Accelerator | 6 |
| 3.2 Fluence Profiles | 7 |
| 3.3 Graphite Fluence Calorimeter Array | 9 |
| 3.4 Depth Dose Calorimeter | 9 |
| 3.5 Maximum Variation in Experimental Depth Dose Measurement for Nominally Identical Machine Parameters | 11 |
| 3.6 Comparison of Measured and Calculated Deposition Profiles in Aluminum for <4.5> MeV Electrons | 13 |
| 3.7 Comparison Between Measured and Calculated Deposition Profiles in Nickel for <4.5> MeV Electrons | 13 |
| 3.8 Deposition Profile in the Target Configuration <4.5 MeV> Electrons in Aluminum Target Backed With Graphite Calorimeter | 14 |
| 3.9 Maximum Observed Spectral Variation From Shot to Shot: Aluminum Depth Dose Measurements | 14 |
| 3.10 Experimental Configuration for Midplane Spall | 16 |
| 4.1 Microscopic Appearance of Midplane Spall in 6061-T6 Aluminum (Magnified 50X) | 20 |
| 4.2 Appearance of Incipient Cracks Induced by Uniform Energy Deposition (Magnified 50X) | 21 |
| 4.3 Incipient Spall in 6061-T6 Aluminum | 22 |
| 4.4 Spall in 6061-T6 Aluminum | 22 |

ILLUSTRATIONS (cont.)

| <u>Figure</u> | | <u>Page</u> |
|---------------|--|-------------|
| 4.5 | Definition of Peak Average (Normalized) Dose for Deposition Profiles Characteristic of In-Depth Heating | 24 |
| 4.6 | Peak Tensile Stress Contours for Deposition Profiles in Figure 4.5 | 24 |
| 4.7 | Incipient Spall in Alpha Titanium | 25 |
| 4.8 | Spall in Alpha Titanium | 25 |
| 4.9 | Midplane Spall in OFHC Copper, Sheet Stock | 27 |
| 4.10 | Midplane Spall in OFHC Copper, Bar Stock | 27 |
| 4.11 | Midplane Spall in OFHC Copper | 28 |
| 4.12 | Comparison of Microstructures and Appearance of Fracture in Bar and Sheet Stock OFHC Copper (Magnified 50X) | 30 |
| 4.13 | Midplane Spall in 6061-T6 Aluminum | 31 |
| 4.14 | Long Heating Time Effects on Midplane Spall in 0.063-Inch 6061-T6 Aluminum | 32 |
| 4.15 | Typical Preheating Cycle, Shot No. 7099, 0.63-Inch 6061-T6 Aluminum Iron-Constantan Thermocouple, Reference Junction 1.28 MV | 32 |
| 4.16 | Precompression Effects on Midplane Spall in 0.063-Inch 6061-T6 Aluminum | 33 |
| 4.17 | Tandem Mode Interferometer System Offering Simultaneous Displacement, Velocity, and Acceleration Information | 35 |
| 4.18 | Velocity Interferometer Record Obtained on Shot No. 13091 | 36 |
| 4.19 | Free Surface Velocity Records of 6061-T6 Aluminum Sample Subjected to Nearly Uniform Sudden Heating | 36 |

ILLUSTRATIONS (cont.)

| <u>Figure</u> | | <u>Page</u> |
|---------------|---|-------------|
| 4.20 | Microscopic Damage Observed in 6061-T6 Aluminum for Shot No. 13080 (Magnified 50X) | 37 |
| 4.21 | Comparison of Measured and Predicted Response of 6061-T6 Aluminum, Shot No. 13085 | 39 |
| 4.22 | Comparison of Measured and Predicted Response of 6061-T6 Aluminum, Shot No. 13091 | 40 |
| 4.23 | Comparison of Measured and Predicted Response of 6061-T6 Aluminum, Shot No. 13080 | 40 |
| 5.1 | Axial Versus Transverse Stress Paths at the Spall Plane in Plate Impact and Electron Beam Experiments | 46 |
| 5.2 | Dynamic Loading Paths for 6061-T6 Aluminum in Pulsed Electron Beam and Plate Impact Experiments | 49 |
| 5.3 | Thermal Degradation of the Yield Strength for 6061-T6 Aluminum Following Instantaneous Heating | 52 |

ABSTRACT

This report describes the results of an experimental effort in which high-energy pulsed electron beams were used to study dynamic fracture induced by rapid in-depth heating. The work was* performed under the metals portion of the PREDIX program; the materials studied were 6061-T6 aluminum, alpha titanium and OFHC copper. Spallation thresholds for these materials are presented in terms of the absorbed energy required to cause a specified amount of damage as a function of the tensile pulse duration. Differences in the loading paths resulting from plate impact on the one hand and rapid in-depth heating on the other hand are also described.

*Contract No. DASA 01-68-C-0138

SECTION 1
INTRODUCTION

SECTION 1

INTRODUCTION

Physics International Company's role in the metals portion of the PREDIX Program was to provide data on dynamic fracture induced by rapid in-depth heating in support of the modeling effort. Specifically, the objectives of the electron beam experiments were to assess the effects of heating rate on the spall strength as well as to obtain spall threshold data under boundary conditions basically different from those that apply to plate impact. Data of this type are pertinent to in-depth heating problems as well as to front surface spall induced by energy deposition.

Techniques were developed in the course of the program to characterize the response of metals to uniform energy deposition. Concurrent improvements in electron beam technology and diagnostics now permit measurements of spall thresholds in a relatively routine manner.

The following sections describe the techniques used and results obtained in examining the effects of in-depth heating in 6061-T6 aluminum, alpha titanium, and OFHC copper.

SECTION 2
MATERIAL CHARACTERIZATION

SECTION 2

MATERIAL CHARACTERIZATION

No material characterization experiments per se were performed. The metals studied in the PREDIX program were standard materials insofar as they had been used for relatively long times in structural and other applications. Consequently, processing techniques are well established and the effects of processing variables are well documented. Although spurious effects that could be ascribed to batch-to-batch variations in material properties were observed in some experiments, these effects were not deemed sufficiently important to warrant a systematic evaluation. Of particular concern were the material properties required (1) to design the in-depth heating experiments, (2) to calculate the energy absorbed by the target, and (3) to analyze and reduce the experimental results to a useful format for those contractors doing fracture modeling.

These properties are the normal density, which in each case is a well known quantity; to a lesser extent, these properties include equation-of-state and material strength data for the appropriate range of pressures, temperatures, and heating rates. This latter type of data, to the extent that it is available, was obtained from the RADS Handbook (Reference 1) or from within PREDIX.

SECTION 3

EXPERIMENTAL TECHNIQUE

SECTION 3

EXPERIMENTAL TECHNIQUE

3.1 THE ELECTRON BEAM ACCELERATOR AND BEAM ENVIRONMENTS

The electron beams used in the bulk of this program^{*} were generated by the Model 1140 Pulserad. The pulsed electron beam environments that can be produced by this accelerator are detailed in Table 3.1. A schematic of the accelerator is shown in Figure 3.1.

A high voltage power supply charges a capacitor bank in parallel. The accelerator is fired by switching to a series configuration, which raises the voltage and decreases the discharge time by closing a series of spark gaps. The voltage surge is used to resonance charge a coaxial transmission line (Blumlein) which delivers a high voltage negative pulse to the cathode. The large electric field at the cathode, consisting of a closely spaced, circular array of needles, results in direct field emission of electrons towards the anode. The electrons pass through the anode, which is a 0.002-inch titanium foil, into a drift chamber where experiments are performed. The partial pressure of air in the drift chamber is adjusted to

^{*} A limited number of pressure-energy coupling and rear surface spall experiments in 6061-T6 aluminum were performed at <1 MeV> on the 738 Pulserad. These are described in Appendix D.

TABLE 3.1

1140 PULSERAD ELECTRON BEAM ENVIRONMENTS

| Mean Electron Energy (MeV) | FWHM Pulse Duration (nsec) | Peak Normalized Dose ($\frac{\text{cal/g}}{\text{cal/cm}^2}$) | Highest Dose Conditions | | | Lowest Dose Conditions | | |
|-------------------------------------|-------------------------------------|--|----------------------------------|---|------------------------------------|----------------------------------|---|------------------------------------|
| | | | Fluence (cal/cm^2) | Uniformly Irradiated Area (cm^2) | Peak Dose (cal/g) | Fluence (cal/cm^2) | Uniformly Irradiated Area (cm^2) | Peak Dose (cal/g) |
| 2 | 60 | 1.5 | 200 | 2 - 3 | 300 | 10 | 10 | 15 |
| 3 | 60 | 1.0 | 300 | 2 - 3 | 300 | 10 | 10 | 10 |
| 4.5 | 60 | 0.50 | 400 | 1 - 2 | 200 | 10 | 10 | 5 |

* For intermediate dose conditions, the size of the uniformly irradiated area is approximately 10 cm^2 .

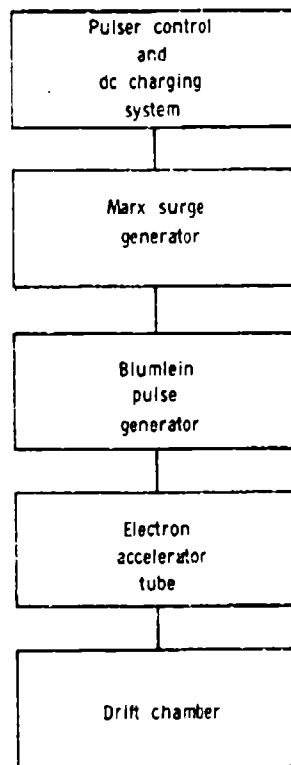


Figure 3.1 Block diagram of accelerator.

produce a stable drifting beam. The beam is slightly divergent as it emerges from the anode and its intensity falls off as the inverse square of the distance from the anode. Several intensity profiles, about the center of the beam, are shown in Figure 3.2 as a function of distance from the anode. Varying the anode to target distance is the most common way of varying the fluence incident on a target.

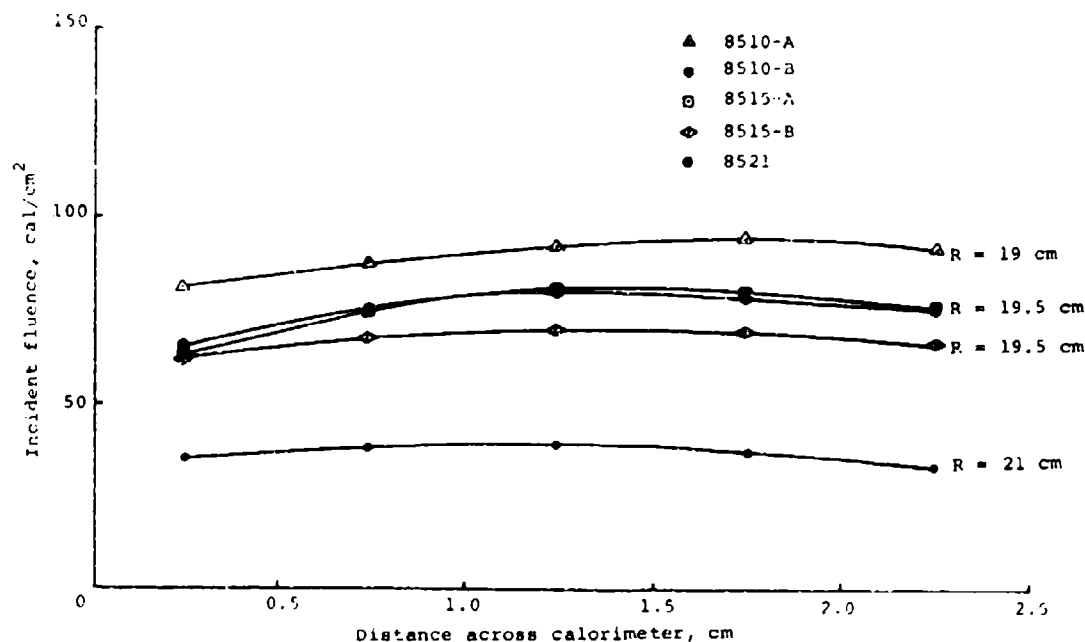


Figure 3.2 Fluence profiles.

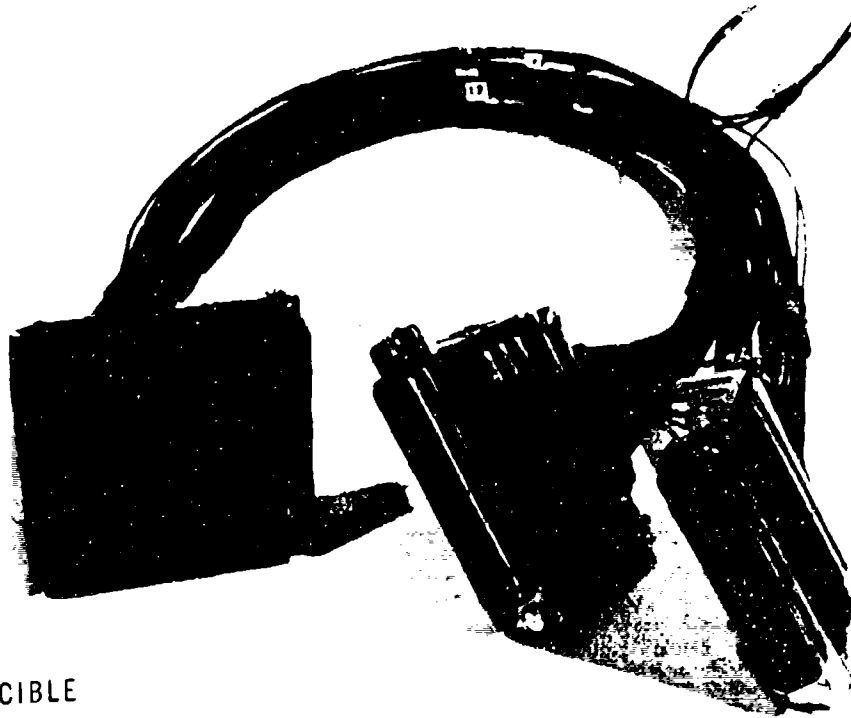
Of particular importance to material response studies is the area over which the incident fluence is uniform (or nearly so). As shown in Table 3.1, this area varies from one or more square centimeters at the highest fluence to ten or more square centimeters at the lowest fluences.

The experiments described in this report were performed using an electron spectrum having a mean energy of 4.5 MeV. At this energy, it was possible to subject the widest range of target thicknesses to uniform deposition while remaining well within the peak dose capabilities of the accelerator. Lower energy electron spectra and correspondingly higher peak dose values that still result in uniform heating (but over a narrower range of target thicknesses) can be obtained using smaller anode-cathode spacings.

3.2 ELECTRON BEAM DIAGNOSTICS AND CALORIMETRY

This section describes the experimental techniques used to measure electron deposition profiles and fluences on the Model 1140 Pulserad for the experiments here under consideration. Additional computational steps required to arrive at a dose in the target are also presented.

In uniform heating experiments the target thickness is less than the electron range and a significant portion of the incident fluence is transmitted through the sample. This transmitted fluence is measured using a segmented graphite calorimeter array, of the type shown on Figure 3.3, located immediately behind the sample. The length of the individual graphite blocks in the array is that required to totally absorb the transmitted beam. The areal dimensions of the blocks are chosen according to the resolution that is required. Typical dimensions used in this work were 1/2 cm x 1/2 cm x 1/2 inch.



NOT REPRODUCIBLE

Figure 3.3 Graphite fluence calorimeter array.

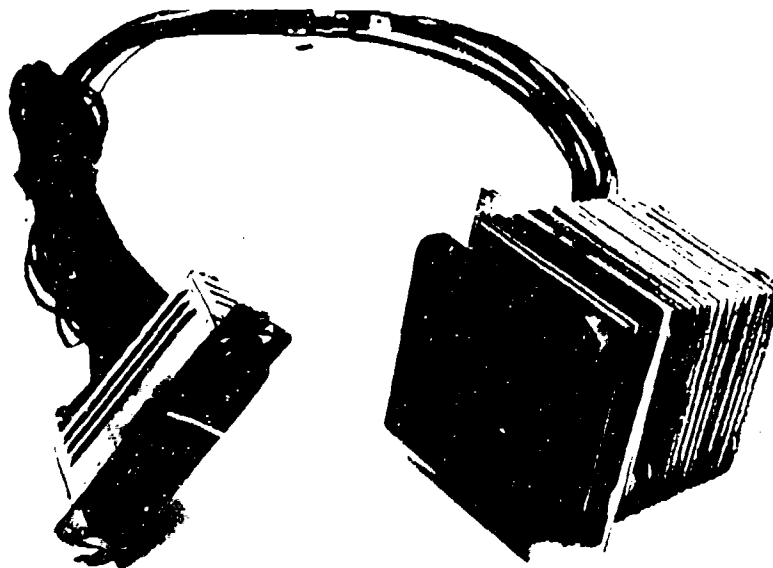


Figure 3.4 Depth dose calorimeter.

Iron-constantan thermocouples are attached to the rear of the graphite blocks with aluminum screws. The temperature rise of the blocks due to deposition is recorded with a high-speed, scanning digital voltmeter. A desk computer is then used to reduce the voltage output to fluences. These calorimeters are believed to be accurate to approximately 5 percent. Figure 3.2 shows several fluence profiles measured with these calorimeters.

Time-integrated energy deposition profiles are measured experimentally using a calorimeter composed of a stack of thin metal foils. One such depth-dose calorimeter is shown in Figure 3.4. The plates are 0.020-inch-thick aluminum and are insulated from each other by 0.060-inch spacers. This spacing minimizes the number of electrons laterally scattered out of the stack. There are 22 plates which are sufficient to stop all the electrons in a 4.5-MeV beam. A collimator defines the incoming beam of electrons so that a circular area about the center of each foil is heated. Thermocouples at the edge of each foil measure the temperature rise which, from the known thermodynamic properties of the foil material, is converted to dose normalized to unit incident fluence.

The results of several depth dose shots using an aluminum foil calorimeter, for nominally identical accelerator conditions, are shown superimposed on Figure 3.5. Accuracy appears to be better than 5 percent.

The accelerator voltage and current traces, respectively, determine the energy spectrum and intensity of the beam. Deposition profiles can also be calculated using electron transport codes and the output of the accelerator voltage and current monitors. The absolute calibration of these monitors is a

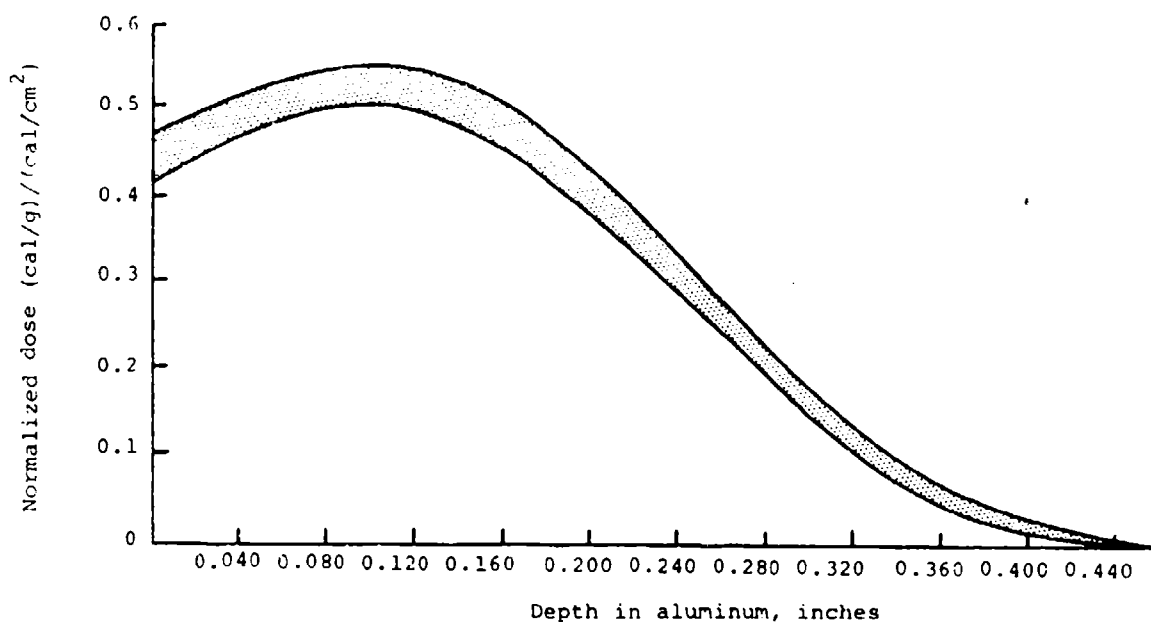


Figure 3.5 Maximum variation in experimental depth dose measurement for nominally identical machine parameters.

difficult task that has not yet been completed. Although this is a drawback, it is not a serious one. Since the electron energy is linearly related to the accelerating voltage, one need only find the correct scaling constant. This is accomplished by using an iterative procedure wherein a scaling factor is assumed and a deposition profile corresponding to this electron spectrum is computed. When the agreement between the experimental and computed deposition profiles is satisfactory, one assumes that the correct scaling factor or electron spectrum has been determined. An absolute calibration of the current monitor is not required. In computing a normalized deposition profile, only the relative intensities over the energy spectrum must be known.

The fact that deposition profiles can be calculated from the accelerator diagnostics is important since it is generally impractical to directly measure time integrated dose in the target. In addition, time-dependent measurements of deposition are clearly beyond the capabilities of current calorimetric techniques.

The degree of correlation that can be obtained between experimental depth dose shots and Monte Carlo code (Reference 2) calculations using the accelerator current and voltage outputs is illustrated in Figures 3.6 and 3.7 for aluminum and nickel calorimeters, respectively. The fact that the time-integrated profiles are in good agreement is taken to mean that the computed time dependence is also essentially correct.

The deposition profiles measured by the previously described depth dosimeters are those for semi-infinite homogeneous medium. In the experimental configuration, however, a finite thickness sample is placed in front of the graphite calorimeter array and this influences the deposition profile. In particular, graphite has a lower atomic number than the materials studied here which results in fewer electrons being back-scattered into the target. The corresponding effects on the deposition profile are illustrated qualitatively in Figure 3.8.

The preceding remarks lead directly to the procedure used to determine the dose absorbed by the target. Deposition profiles in aluminum depth dosimeters are measured by spanning the range of accelerator outputs encountered in the spall shots. Electron energy spectra for these shots are determined as previously described (the spectrum varies somewhat from shot to shot as illustrated in Figure 3.9). Once the electron spectrum

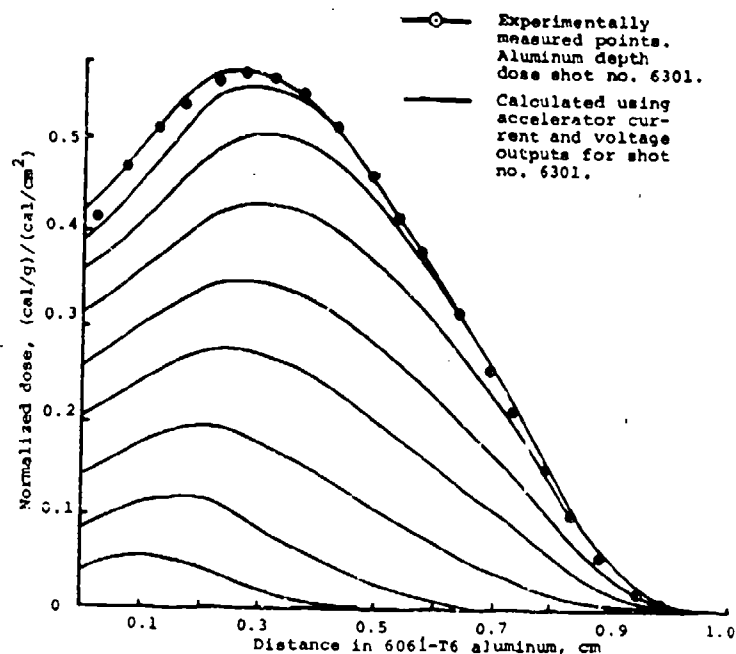


Figure 3.6 Comparison of measured and calculated deposition profiles in aluminum for $<4.5 \text{ MeV}>$ electrons.

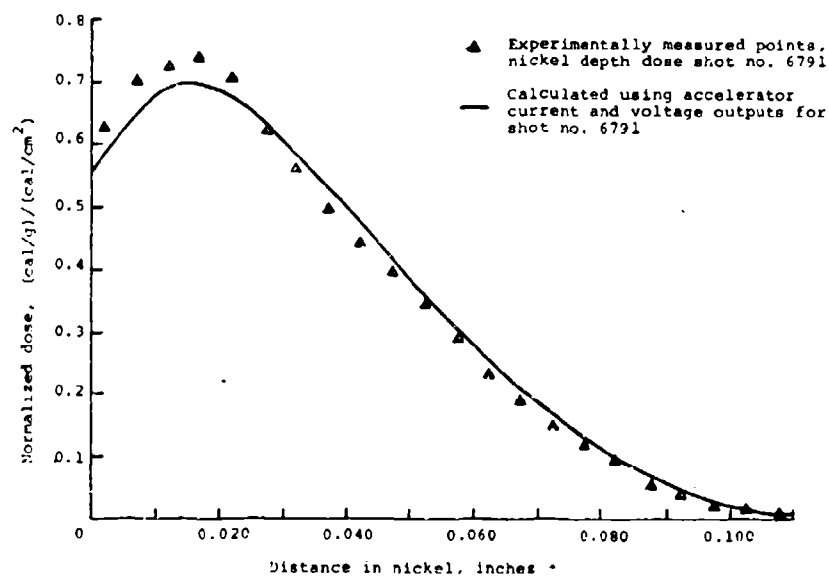


Figure 3.7 Comparison between measured and calculated deposition profiles in nickel for $<4.5 \text{ MeV}>$ electrons.

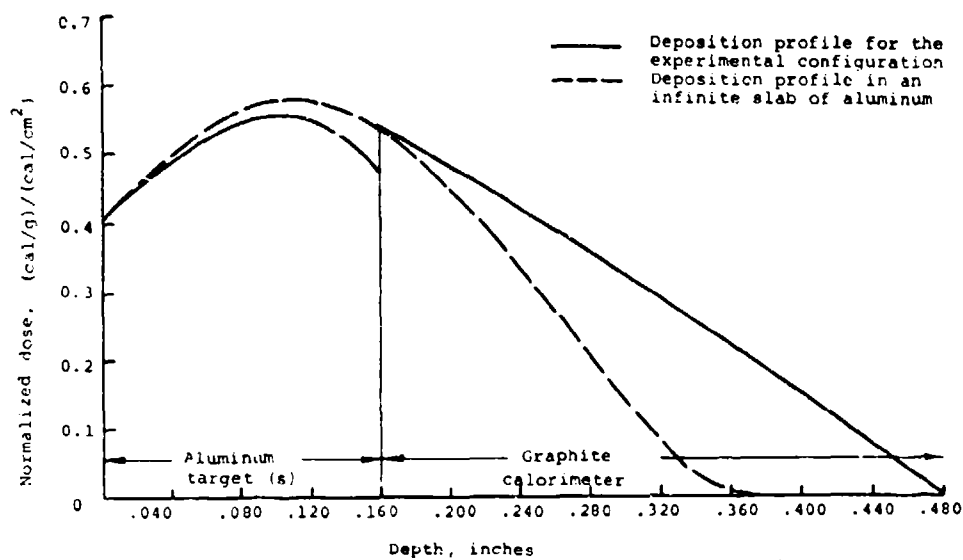


Figure 3.8 Deposition profile in the target configuration
4.5 MeV electrons in aluminum target backed
with graphite calorimeter.

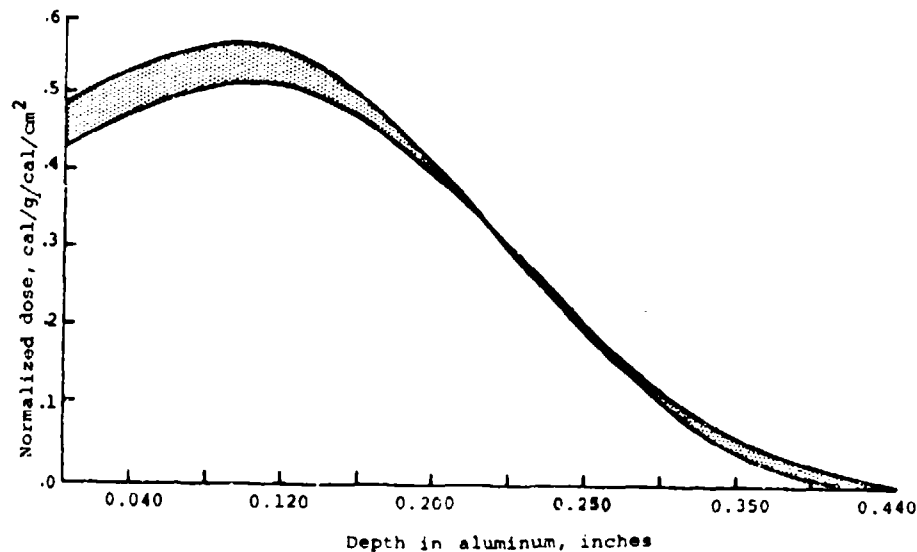


Figure 3.9 Maximum observed spectral variation from shot to
shot: aluminum depth dose measurements.

is known, the Monte Carlo code (Reference 2) is used to calculate the deposition profile for the actual target configuration (i.e., spall specimen(s) backed with graphite).

3.3 PROCEDURE FOR DETERMINING SPALL THRESHOLDS

The electron beam environments are selected on the basis of maximum sample thickness that is to be uniformly heated and an estimate of the peak dose levels that will be required to bracket the spall thresholds. Thick targets (or high-Z materials) require relatively high energy electrons (3 to 5 MeV) for uniform deposition. In targets so thin that there is appreciable pressure relief during deposition, considerably lower energy electrons may be required to attain the dose values for spall. In the present program it was found that <4.5 MeV> electron beams could be used to explore spall phenomena over the full range of interest.

The experimental configuration for in-depth shock heating experiments is shown in Figure 3.10. The targets are slabs of uniform thickness and have approximately 1.5 inches x 1.5 inches lateral dimensions (these dimensions are not critical). Depending on the thickness, one or more stacked slabs can be irradiated simultaneously. The natural fall-off in the deposition profile can thus be used to provide more than one dose level per exposure. The thickness of each slab and the number of slabs in the stack must, of course, be chosen so that each slab is uniformly heated (or nearly so).

After exposure the specimens are cut along a line through the peak of the fluence profile, polished, and examined metallographically for damage. Incipient spall is defined as all damage

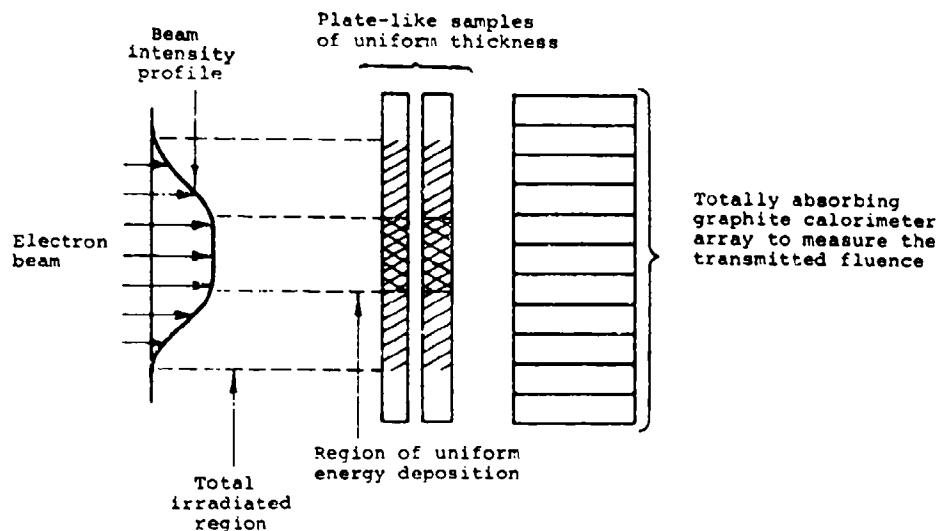


Figure 3.10 Experimental configuration for midplane spall.

consisting of cracks whose individual length is less than 1 mm. The onset of incipient spallation, as evidenced by the first appearance of cracks visible at 50X, is defined as the damage-no damage threshold. It is further considered that complete spall has occurred whenever the length of individual cracks is equal to or greater than 1 mm.

The crossover point is the complete spall threshold. It is observed that crack coalescence becomes increasingly important for crack lengths greater than 1 mm and that, in addition, the material is so severely damaged at this point that strength in tension, perpendicular to the spall plane, is very small.

It is recognized that other reasonable definitions of spall threshold exist. The ones that have been adopted, however, give the best correlation between absorbed dose and observed damage for in-depth heating experiments. The damage-no damage threshold, in particular, is physically realistic and most widely applicable because it is independent of details such as crack orientation and concentration.

Finally, on subsequent exposures, the levels are varied until the spall thresholds have been bracketed to the desired accuracy.

SECTION 4
EXPERIMENTAL RESULTS

SECTION 4

EXPERIMENTAL RESULTS

The results of midplane spall experiments on as-received 6061-T6 aluminum, alpha titanium, and OFHC copper (bar and sheet stock) are presented in this section. For these experiments the targets were initially at room temperature. Also reported are (1) more limited sets of experiments on 6061-T6 aluminum pre-heated (long soak times) to various temperatures immediately before irradiation and (2) experiments on 6061-T6 aluminum targets subjected to a prior compressive shock.

The microscopic appearance of midplane spall is illustrated in Figures 4.1 and 4.2. As previously noted, damage is correlated with the peak absorbed dose and the results are then plotted as a function of target thickness as shown for 6061-T6 aluminum in Figures 4.3 and 4.4. The spall thresholds are sharply defined.

Acoustically thin targets are those in which there is relief of pressure during the deposition time (approximately 60 nsec FWHM or 100 nsec total). Higher dose levels are accordingly required to develop the tensile stresses or strains to cause fracture. It is also to be noted that temperature varies along the threshold dose curves.

There is some ambiguity in the definition of dose in a sample that is so thick, or is so positioned in the stack that the deposition profile has some fall-off. This situation, together with a definition of peak average dose, is shown in

Shot no. 7109-1A



Beginning of spall

Shot no. 7099-1A



Intermediate incipient spall

Shot no. 7114



Intermediate incipient spall

Shot no. 7095-1A



Advanced incipient spall

Shot no. 7098-1B



Advanced incipient spall

Shot no. 7104-2B



Complete spall

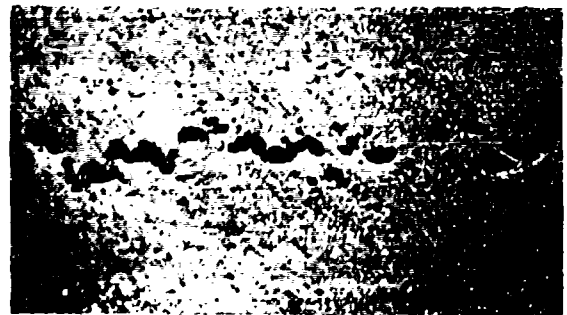
Figure 4.1 Microscopic appearance of midplane spall in 6061-T6 aluminum (magnified 50X).

Shot no. 5698



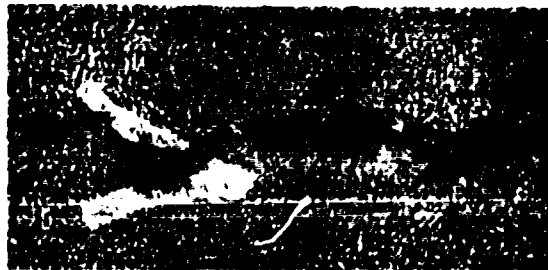
6061-T6 aluminum initially
at room temperature

Shot no. 8134-2



6061-T6 aluminum preheated
for 16 minutes at 400 F

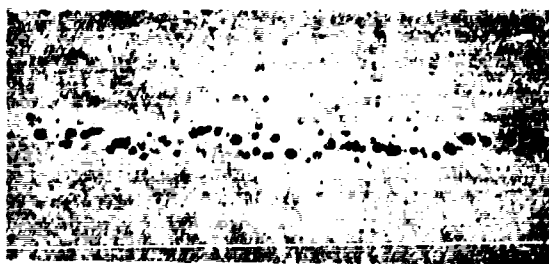
Shot no. 5925



Alpha titanium

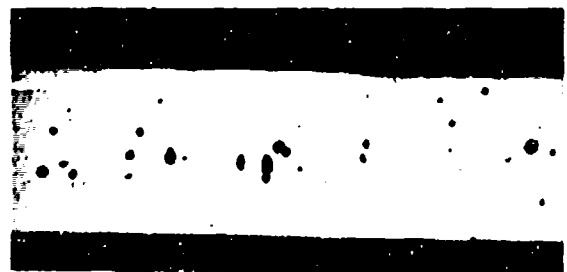
NOT REPRODUCIBLE

Shot no. 6764-1



OFHC copper sheet stock

Shot no. 6771-5



OFHC copper bar stock

Figure 4.2 Appearance of incipient cracks induced by uniform
energy deposition (magnified 50X).

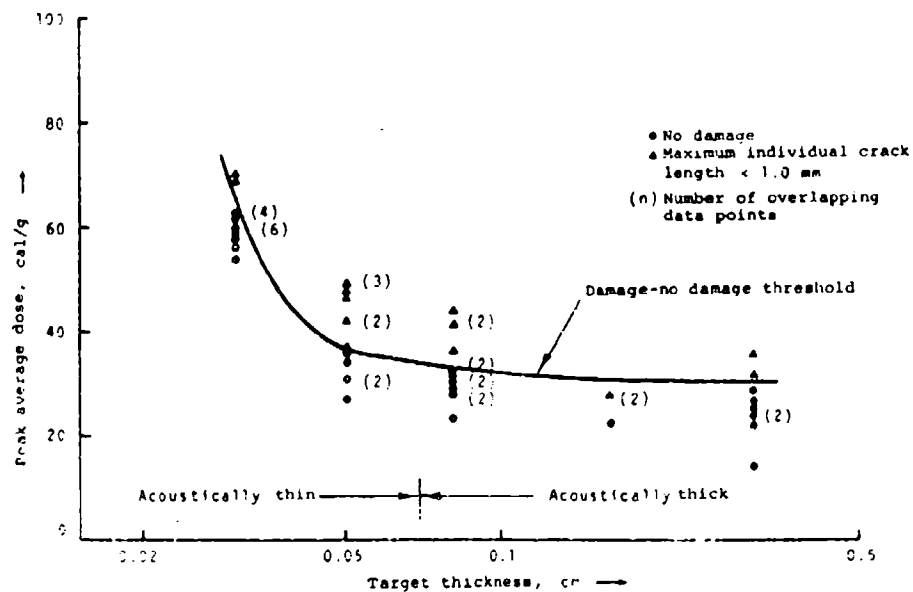


Figure 4.3 Incipient spall in 6061-T6 aluminum.

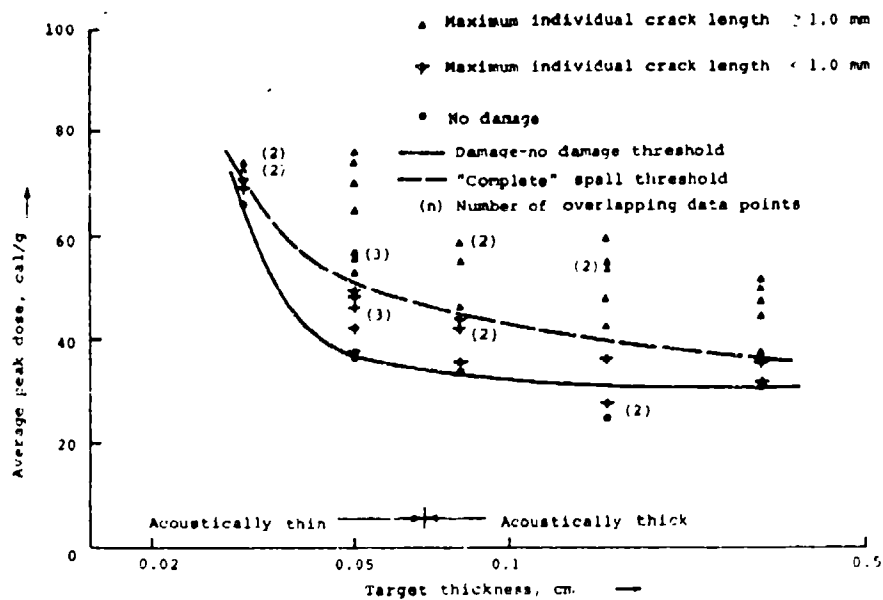


Figure 4.4 Spall in 6061-T6 aluminum.

Figure 4.5. The results that have been obtained indicate that even an appreciable fall-off dose does not lead to scatter or inconsistencies in the spall thresholds. Computations that support this conclusion have been performed. For example, Figure 4.6 shows the peak tensile stress profiles corresponding to the two deposition profiles on Figure 4.5. Although differences exist they are not dramatic.

Table 4.1 lists the threshold values obtained for 6061-T6 aluminum. Some of these have been interpolated from the shots nearest to the spall threshold. For material response calculations, it is suggested that deposition profiles and fluences for the shots nearest to the spall threshold be used. These shots are listed in Table 4.1; accompanying deposition profiles and fluences are contained in Appendix A. At the higher fluence levels the radial fall-off in fluence over the irradiated area of the sample can be appreciable. However, the fall-off about the peak of the fluence distribution over distances comparable to the target thickness is always very small. The peak fluence, there, is the appropriate quantity for 1-D calculations.

TABLE 4.1
EFFECTS OF UNIFORM ENERGY DEPOSITION IN 6061-T6 ALUMINUM
INITIALLY AT ROOM TEMPERATURE

| Sample Thickness (inch) | Damage-No Damage Threshold Dose (cal/g) | Complete Spall Threshold Dose (cal/g) | Experimental Shot Nearest To Damage-No Damage Threshold | Complete Spall Threshold |
|-------------------------|---|---------------------------------------|---|--------------------------|
| 0.012 | 66.0 | 72.0 | 5916-6 | 5916-4 |
| 0.020 | 36.5 | 51.0 | 5853-5 | 5855-4 |
| 0.032 | 35.0 | 43.0 | 5858-3 | 5905-2 |
| 0.063 (Batch 1) | 25.5 | 32.0 | 5911-1 | 5860-1 |
| 0.063 (Batch 2) | 41.0 | 51.0 | 8522-2 | 8523-1 |
| 0.125 | 32.0 | 38.0 | 5698-1 | 5693-1 |

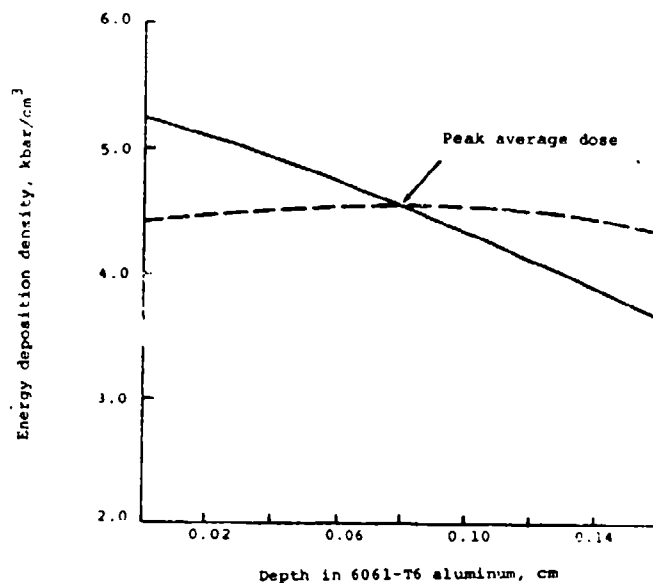


Figure 4.5 Definition of peak average (normalized) dose for deposition profiles characteristic of in-depth heating.

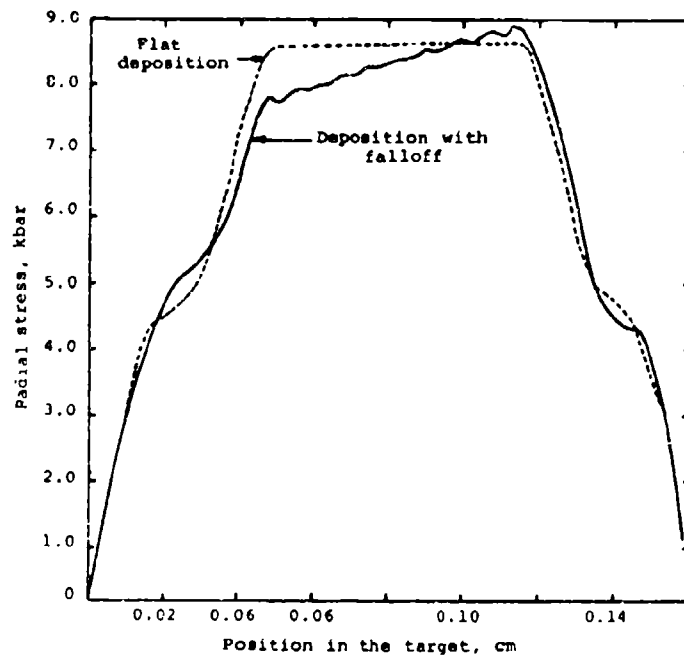


Figure 4.6 Peak tensile stress contours for deposition profiles on Figure 4.5.

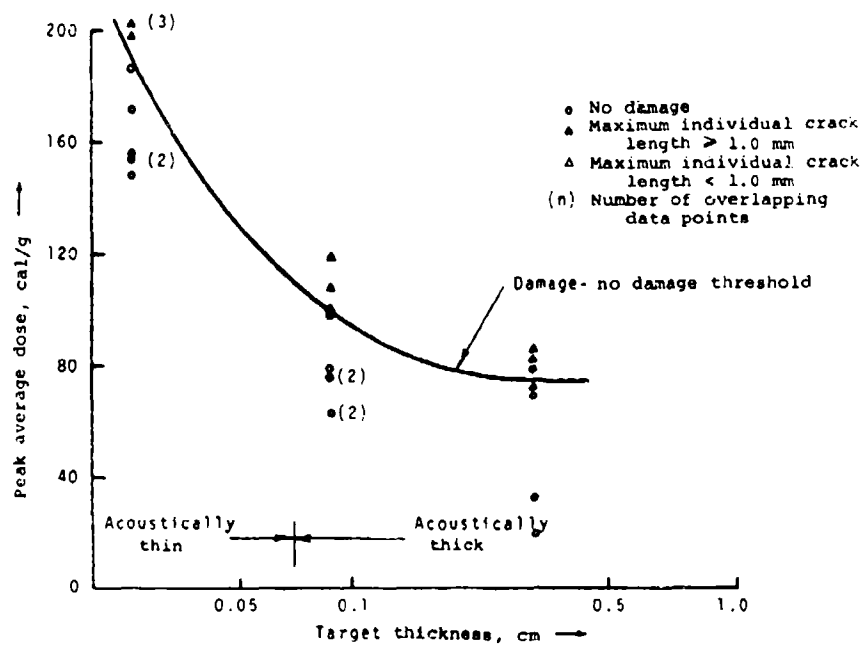


Figure 4.7 Incipient spall in alpha titanium.

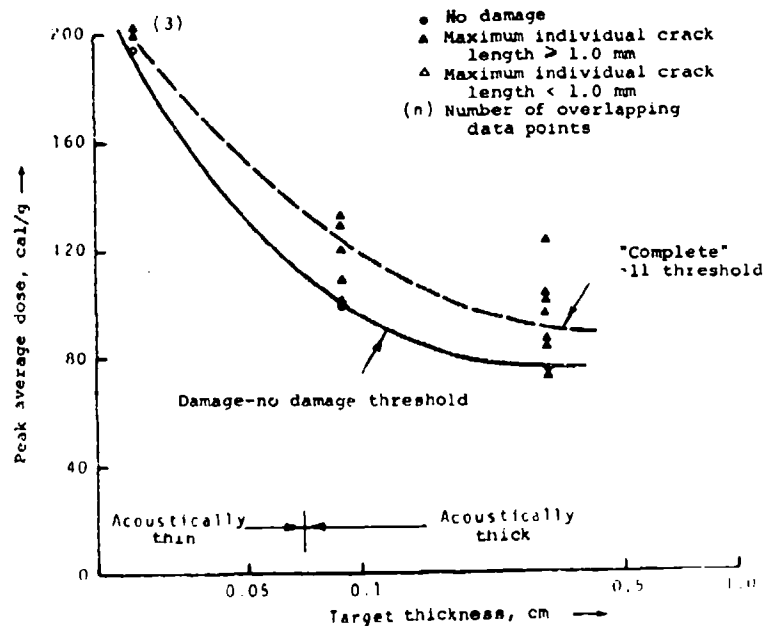


Figure 4.8 Spall in alpha titanium.

The results for alpha titanium are shown in Figure 4.7 and 4.8. Table 4.2 summarizes the results. Energy deposition parameters appear in Appendix B. As can be expected, the qualitative trends in the threshold dose versus target thickness relations are the same as in aluminum. Calculations involving threshold dose levels above 120 cal/g must consider the effects of the $\alpha(\text{hcp}) \rightarrow \beta(\text{bcc})$ transformation that begins at 870 C. There is evidence that this transformation can occur on a microsecond time scale (Reference 3).

TABLE 4.2
EFFECTS OF UNIFORM ENERGY DEPOSITION IN
ALPHA TITANIUM INITIALLY AT ROOM
TEMPERATURE

| Sample Thickness (inch) | Damage-No Damage Threshold Dose (cal/g) | Complete Spall Threshold Dose (cal/g) | Experimental Shot Nearest to: | |
|----------------------------|---|---|----------------------------------|--------------------------------|
| | | | Damage-No Damage Threshold | Complete Spall Threshold |
| 0.009 | 192.5 | 192.5 | 5919-5 | 5919-4 |
| 0.035 | 99.5 | 123.0 | 5827-1 | 5830-1 |
| 0.125 | 70.5 | 90.5 | 5821-1 | 5925-1 |

The last set of results to be presented are those on OFHC copper. Both sheet and bar stock were examined. The results are shown in Figures 4.9 through 4.11 and are further summarized in Table 4.3. Energy deposition parameters are presented in Appendix C. These two forms of copper have rather different spall thresholds. Metallographic observations indicate that in sheet stock material, where the direction of grain alignment is parallel to the spall plane, fracture was predominantly intergranular. In the bar stock material the grains were aligned

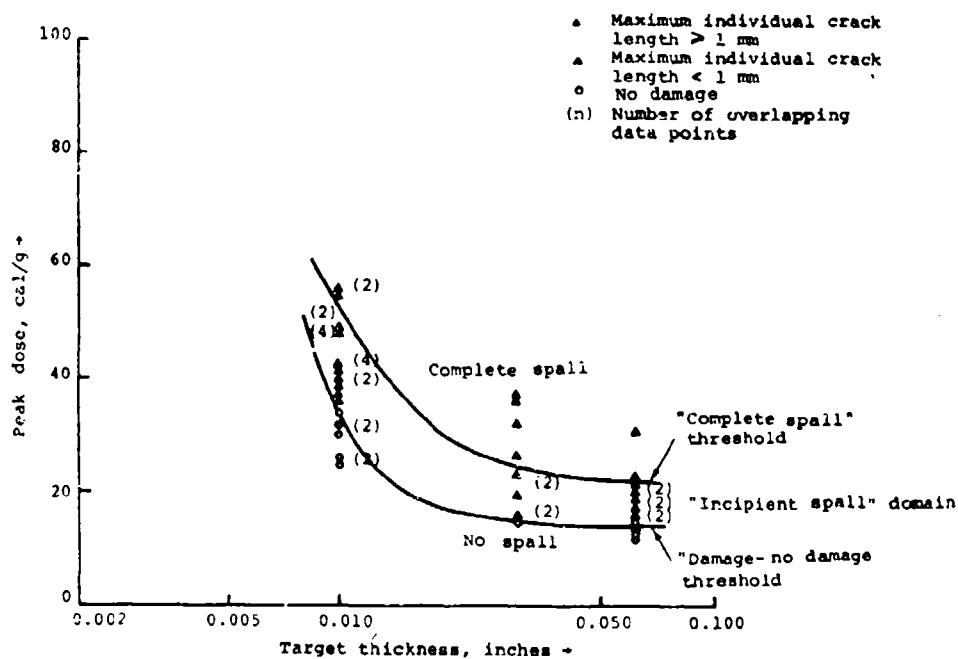


Figure 4.9 Midplane spall in OFHC copper, sheet stock.

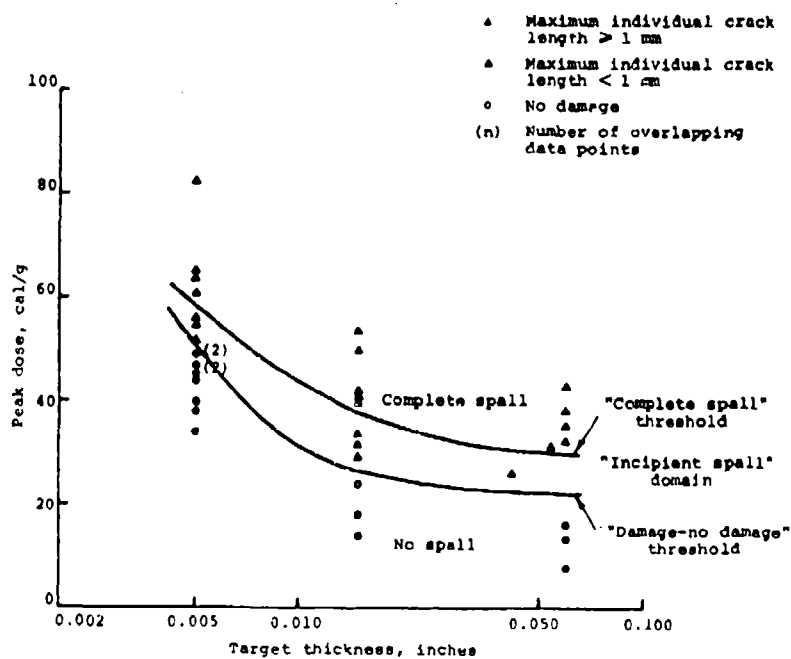


Figure 4.10 Midplane spall in OFHC copper, bar stock.

perpendicular to the spall plane and fracture tended to be transgranular. This is illustrated in Figure 4.12. Differences in ductility with preferred orientation may account for the observed threshold dose behavior.

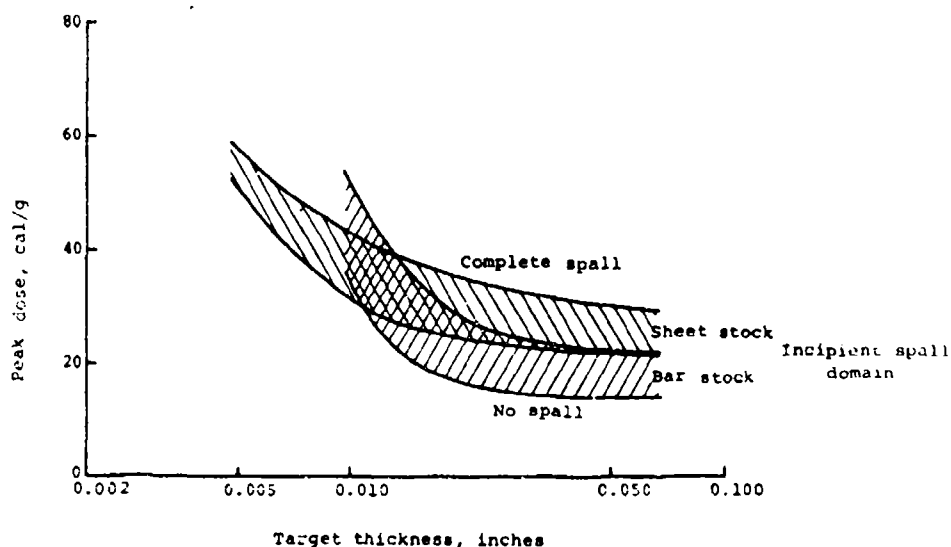


Figure 4.11 Midplane spall in OFHC copper.

As spall threshold data were being generated, comparisons were being made between the computed spall stresses for gas gun and electron beam experiments. These comparisons indicated that fracture induced by in-depth heating was occurring at lower stress levels than in plate impact. This is illustrated in Figure 4.13 which compares the computed peak tensile stress at the spall thresholds for the various experiments in 6061-T6 aluminum. In addition, there is a marked lack of time dependence in the electron beam experiments. These observations apply as well to the other materials studied. It was thought initially that perhaps the material was weaker in the electron beam because spall was occurring at an elevated temperature. The possibility was also raised that the precompressive stress or strain that the spall plane experiences in a plate impact experiment could be strengthening the material.

TABLE 4.3

EFFECTS OF UNIFORM ENERGY DEPOSITION IN OFHC
COPPER INITIALLY AT ROOM TEMPERATURE

| <u>Bar Stock</u> | | | | |
|-------------------------------|---|---|---|--------------------------------|
| Sample Thickness (inch) | Damage-No Damage Threshold Dose (cal/g) | Complete Spall Threshold Dose (cal/g) | Experimental Shot Nearest To Damage-No Damage Threshold | Complete Spall Threshold |
| 0.005 | 50.0 | 58.5 | 6781-3 | 6770-3 |
| 0.015 | 26.5 | 40.0 | 6292-1 | 6770-5 |
| 0.060 | 21.0 | 29.0 | 6285-1 | 6287-1 |
| <u>Sheet Stock</u> | | | | |
| 0.010 | 33.0 | 52.0 | 6534-3 | 6536-2 |
| 0.030 | 15.0 | 24.5 | 6530-1 | 6763-1 |
| 0.063 | 12.5 | 21.5 | 6524-1 | 6524-1 |



Bar stock

Virgin
material



Sheet stock

Appearance of fracture



Shot no. 6768, 30.6 cal/g peak dose, 0.062-in. copper sheet stock



Shot no. 6771, 29.0 cal/g peak dose, 0.015-in. copper bar stock

Figure 4.12 Comparison of microstructures and appearance of fracture in bar and sheet stock OFHC copper (magnified 50X).

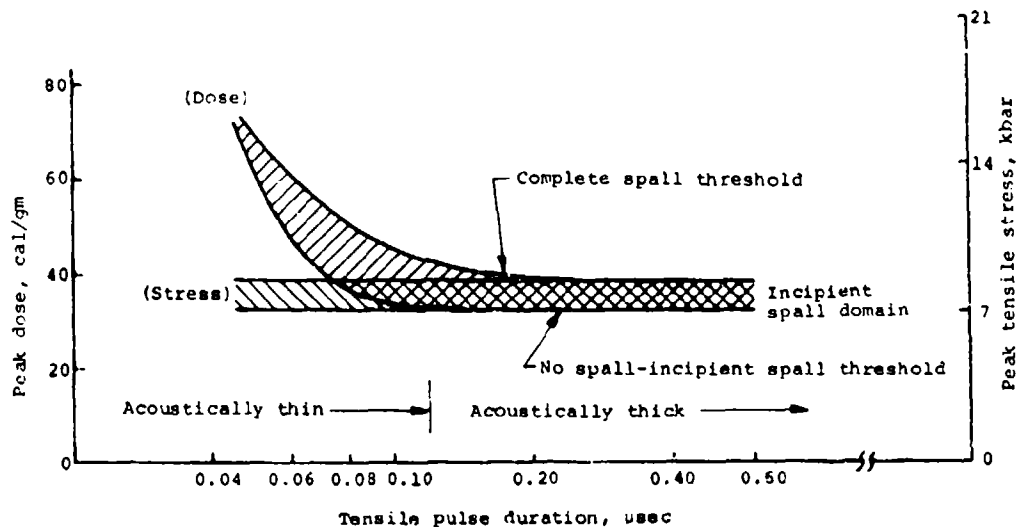


Figure 4.13 Midplane spall in 6061-T6 aluminum.

The possible effects of temperature and precompression were examined in two brief sets of experiments. In the first of these experiments, 0.063-inch 6061-T6 aluminum targets were preheated to temperatures up to 500 F immediately before irradiation. An oven located in the electron beam chamber was used. Heating times were on the order of 16 minutes and the spall thresholds were determined in the usual manner. The results are shown in Figure 4.14. A typical preheat cycle is shown on Figure 4.15. It appears that temperature has only a modest effect on the threshold dose for spall. Note that the heating due to irradiation further increases the temperature (at approximately 10 F/cal/g) above the soak temperatures.

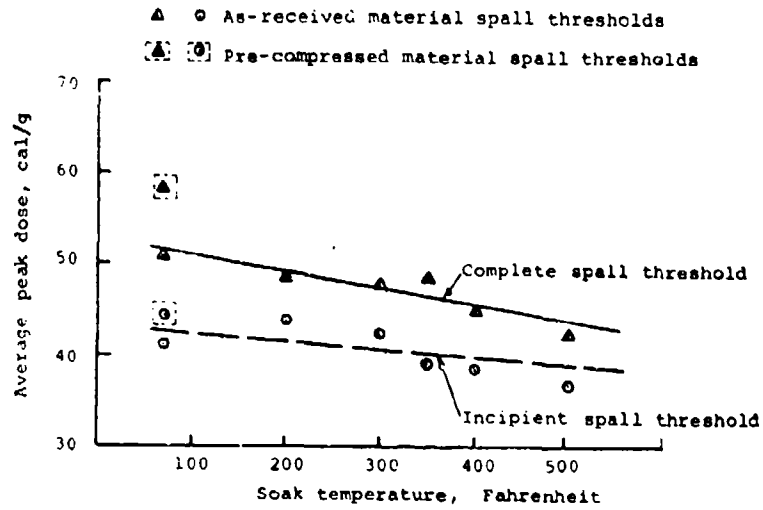


Figure 4.14 Long heating time effects on midplane spall in 0.063-inch 6061-T6 aluminum.

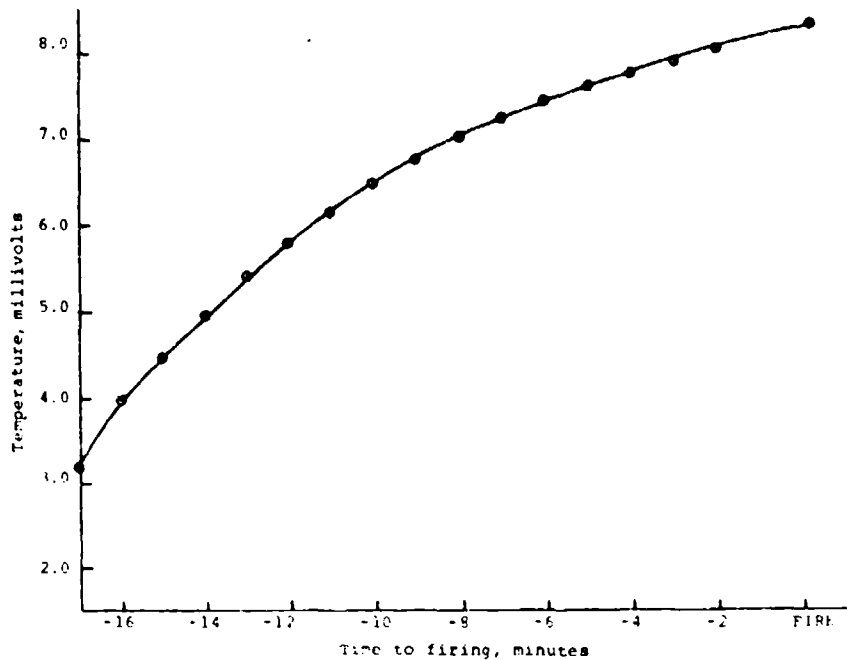


Figure 4.15 Typical preheating cycle, shot no. 7099, 0.063-inch 6061-T6 aluminum iron-constantan thermocouple, reference junction 1.28 MV.

In the second set of experiments, 0.063-inch 6061-T6 specimens were preshocked in the Effects Technology, Inc. exploding foil facility using 0.014-inch Mylar fliers and impact velocities of approximately 0.067 cm/ μ sec. A peak compressive stress of about 22 kbar was thereby introduced in the aluminum samples which were, in addition, protected by momentum traps. The midplane spall thresholds were subsequently determined in the usual manner. The results are summarized in Figure 4.16.

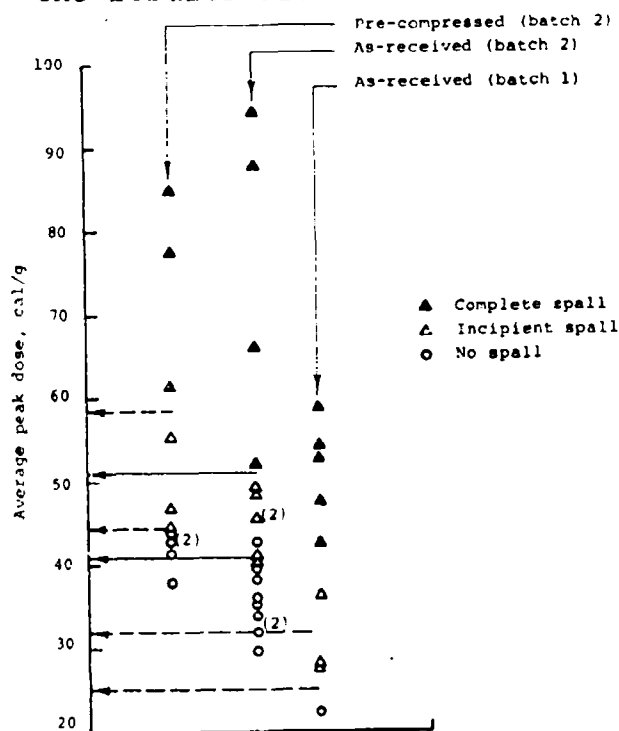


Figure 4.16 Precompression effects on midplane spall in 0.063-inch 6061-T6 aluminum.

The complete spall threshold dose and, to a lesser extent, the incipient spall threshold dose are both raised by precompression. These results refer to only one compressive pulse amplitude and duration. Greater or lesser strengthening may result from different precompressive loads. Another observation is that batch-to-batch variations in material properties

can have an effect on the threshold dose for spall. The magnitude of the effect is illustrated in Figure 4.16 for the 0.063-inch material. Only this thickness of material showed pathological behavior from batch-to-batch.

In addition to the passive shots, a few uniform heating experiments were performed in which the velocity of the free surface was observed with a laser interferometer. The objective of this series of experiments was to provide an independent determination of the stress required to produce spall. Simultaneous measurements of displacement (Reference 4) and velocity (Reference 5) were made.

A difficulty frequently encountered in interpretation of the interferometer records is the detection of the point at which the velocity reverses direction. If this occurs near a maximum or minimum of the fringe intensity, there is often no clear indication of the reversal. The reversals in the displacement record are easier to detect since the individual fringes are distinguishable only when the velocity is less than about 35 m/sec. Thus, by making simultaneous measurements, the times at which the velocity is zero can be obtained from the displacement record. This information then provides a check on the peak velocity since the number of fringes increasing the velocity from zero to the peak must equal the number of fringes decreasing the velocity from the peak to zero.

The interferometer measurements were made on 1/8-inch-thick 6061-T6 aluminum. However, it was not the PREDIX material^{*} since the latter was no longer available at the time these experiments were performed. The experimental configuration is

^{*} In order to minimize uncertainties, all experimenters within PREDIX were supplied with controlled and identical stocks of material.

shown in Figure 4.17. It was necessary to position the photomultiplier tube at a substantial distance from the target and behind considerable shielding to prevent bremsstrahlung radiation from perturbing the output.

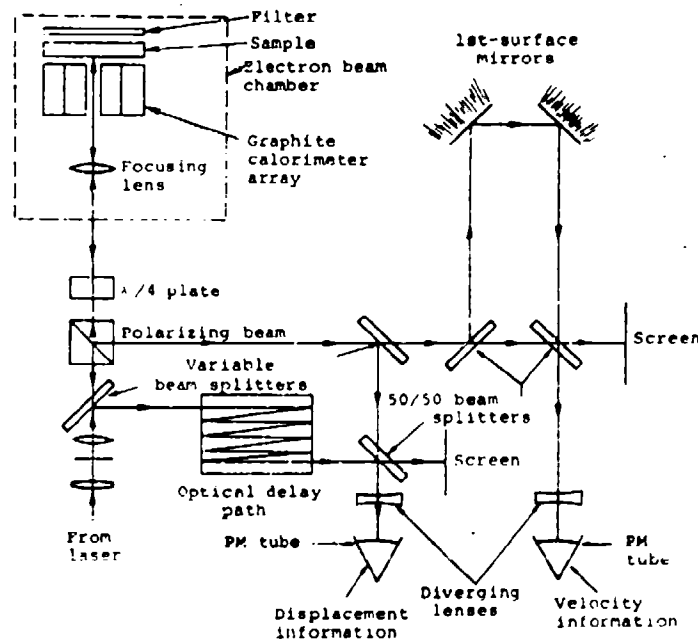


Figure 4.17 Tandem mode interferometer system offering simultaneous displacement, velocity, and acceleration information.

A representative oscilloscope record is shown in Figure 4.18. The velocity time records from several shots are shown in Figure 4.19. Extensive spall occurred on shots number 13080 and 13090. The effect of the spall upon the free surface velocity history is readily seen in Figure 4.19; successive reflections of the pulse occur at the spall plane, reducing the transit time to half the value observed for undamaged material. Although complete separation did not occur, the amount of damage on these shots exceeded the level previously defined as the complete spall threshold. A photomicrograph of the sample for shot number 13080 is shown in Figure 4.20.

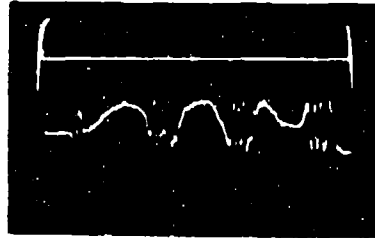


Figure 4.18 Velocity interferometer record obtained on shot no. 13091.

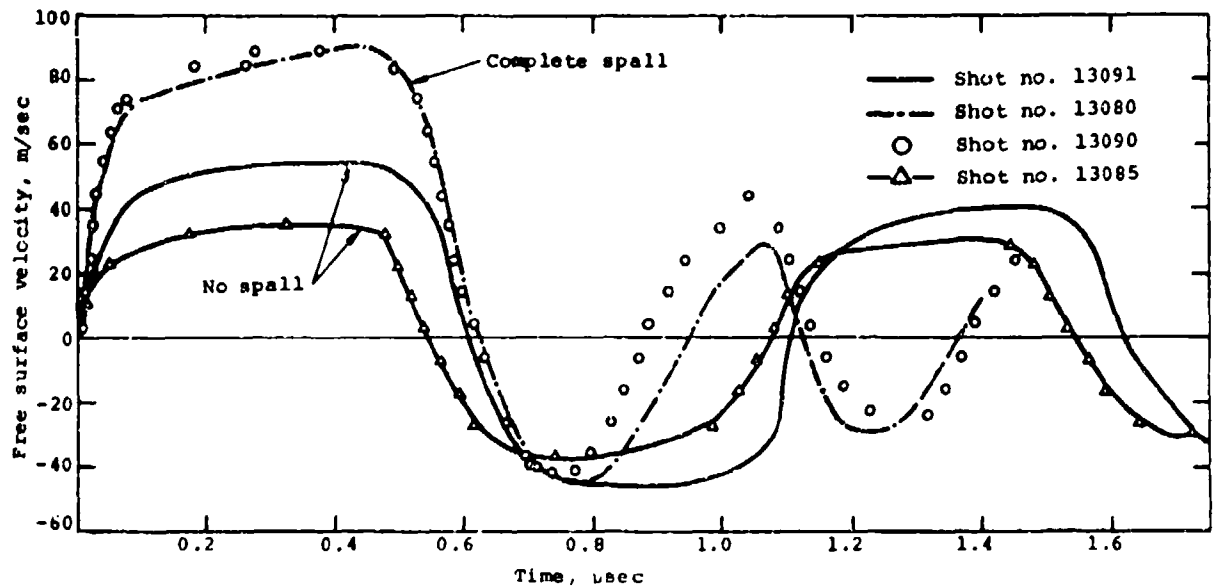


Figure 4.19 Free surface velocity records of 6061-T6 aluminum sample subjected to nearly uniform sudden heating.

NOT REPRODUCIBLE

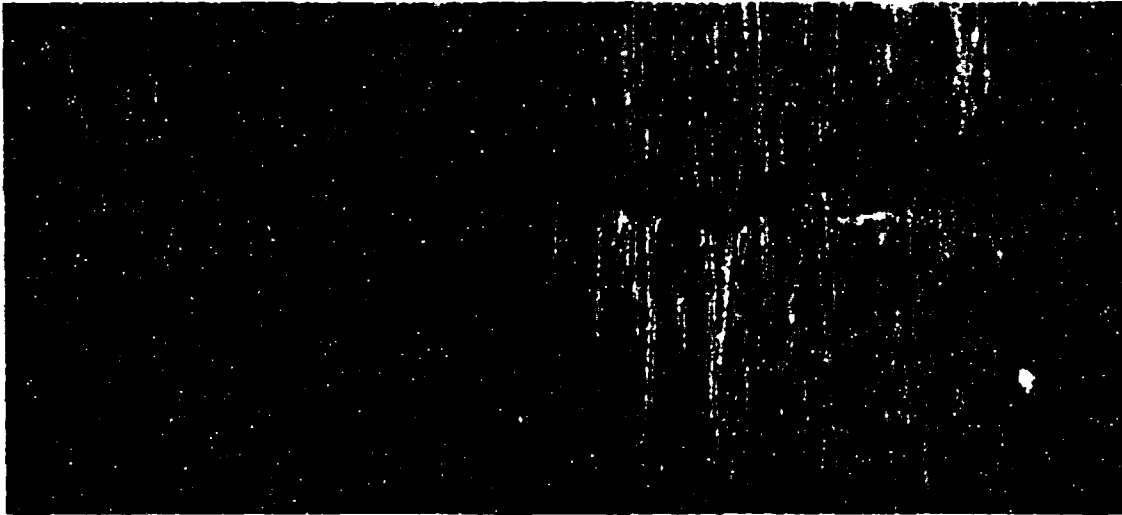


Figure 4.20 Microscopic damage observed in 6061-T6 aluminum for shot no. 13080 (magnified 50X).

Some difficulty was encountered in obtaining an accurate measurement of fluence, since a calorimeter could not be placed directly behind the sample at the point where the velocity was observed. Calorimeters were used to measure the transmitted beam intensity surrounding the observation point; however, several factors complicate the use of these measurements to deduce the fluence incident on the sample. In particular, the absence of the center calorimeter block in the array perturbs the readings of the adjacent blocks. This occurs because electrons scattered laterally into the opening are not replaced by electrons that would otherwise be scattered from the center block into the surrounding blocks. Additional uncertainties arise from estimating the peak intensity from peripheral readings. Finally, in these particular experiments, the recording

time of the scanning digital voltmeter that reads and prints the thermocouple readings was not long enough to allow observation of the peak temperature. Consequently, estimates of the peak dose levels in these experiments based upon the calorimetric measurements were regarded only as lower bounds.

The peak dose, E_m , obtained on each shot can be estimated from the peak observed free surface velocity, u_{fs} , from the relations

$$P_m = \rho \Gamma E_m$$

where ρ is the density and Γ is the Gruneisen coefficient and

$$u_{fs} = \int_{P_0}^0 \left(- \frac{\partial V}{\partial P} \right)_S^{\frac{1}{2}} dP = \int_{P_0}^0 \frac{dP}{\rho c(P,t)}$$

where c is the sound velocity. A knowledge of the energy deposition profile then serves to establish the fluence.

A cross check of the deposition profile is provided by comparing the experimental data with the computed response using the POD^{*} code. Such comparisons are shown for shots number 13085, 13091, and 13080 in Figures 4.21 to 4.23, respectively. In general, close agreement is obtained, except subsequent to the occurrence of the spall in shot number 13080. In this computation, a minimum pressure criterion was used and here the lack of agreement after spall is not an issue of concern. Equation-of-state parameters used in the computation for aluminum were obtained from Reference 6 and Appendix D of this report.

* Physics International's finite difference material response code.

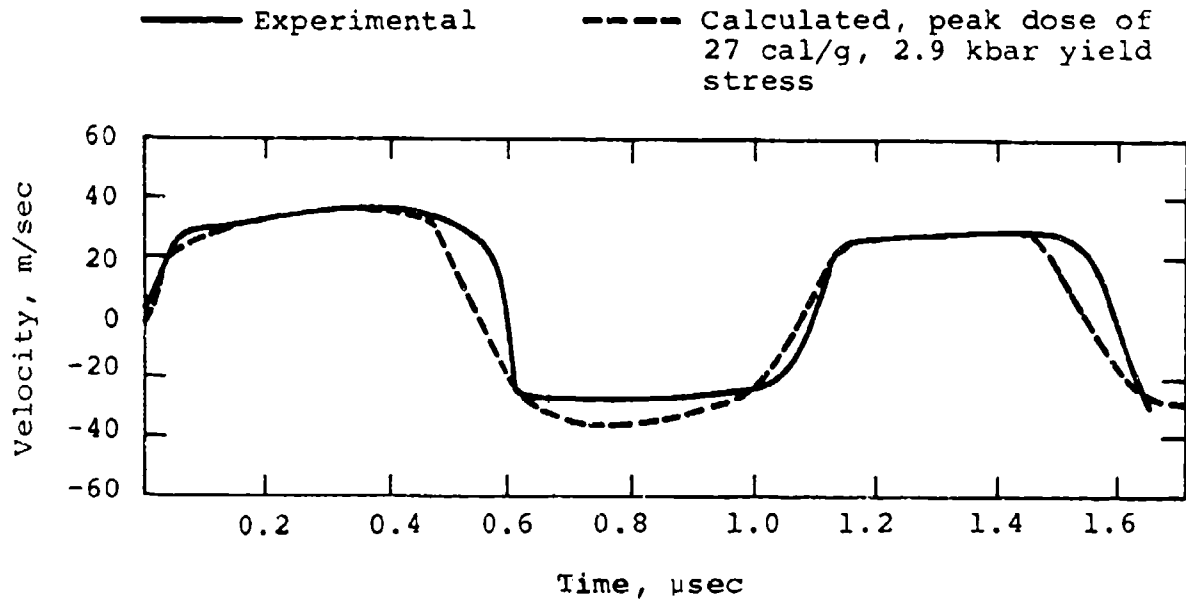


Figure 4.21 Comparison of measured and predicted response of 6061-T6 aluminum, shot no. 13085.

The dose levels predicted by the free surface velocities are approximately 1.7 times greater than those deduced from the calorimetry. This is somewhat disturbing, especially since a discrepancy of this magnitude would largely eliminate the observed differences in spall strength between uniform heating and plate impact experiments.

However, a careful re-examination of the calorimetric techniques used in obtaining the uniform heating spall threshold data tends to discount the possibility of an error of such a large magnitude. These considerations are detailed in Section 5.

Sections of the target materials for shots number 13080 and 13090 revealed damage exceeding the extent that defines the complete spall threshold (i.e., continuous cracks of length

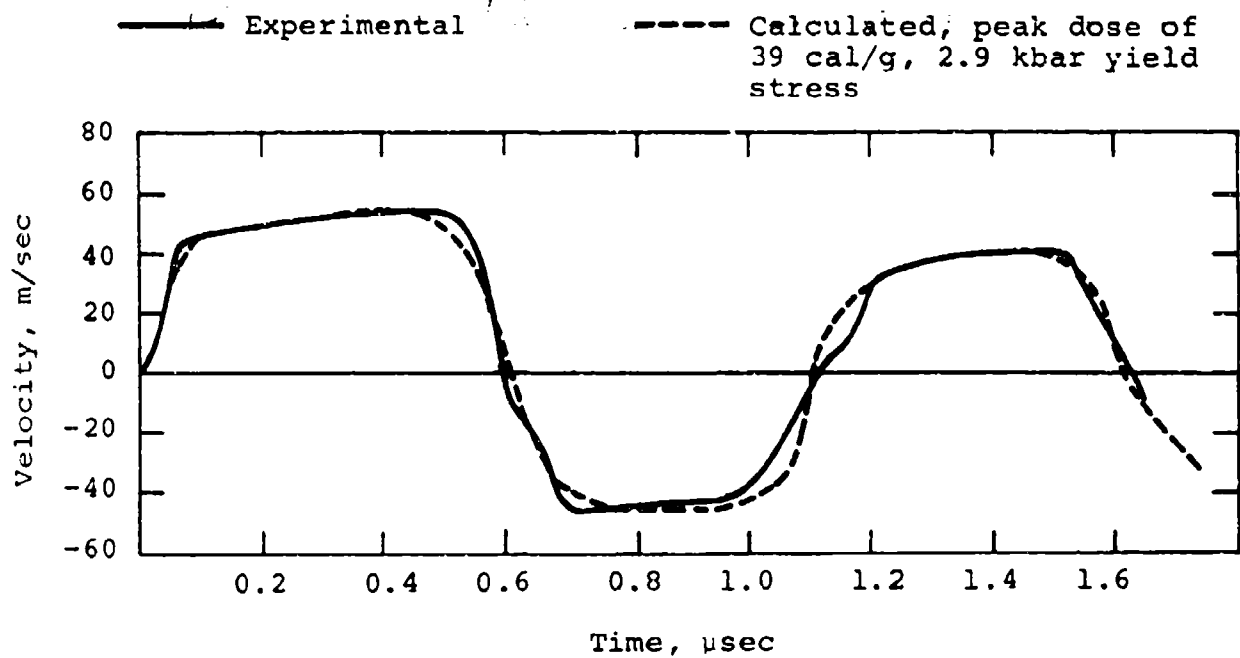


Figure 4.22 Comparison of measured and predicted response of 6061-T6 aluminum, shot no. 13091.

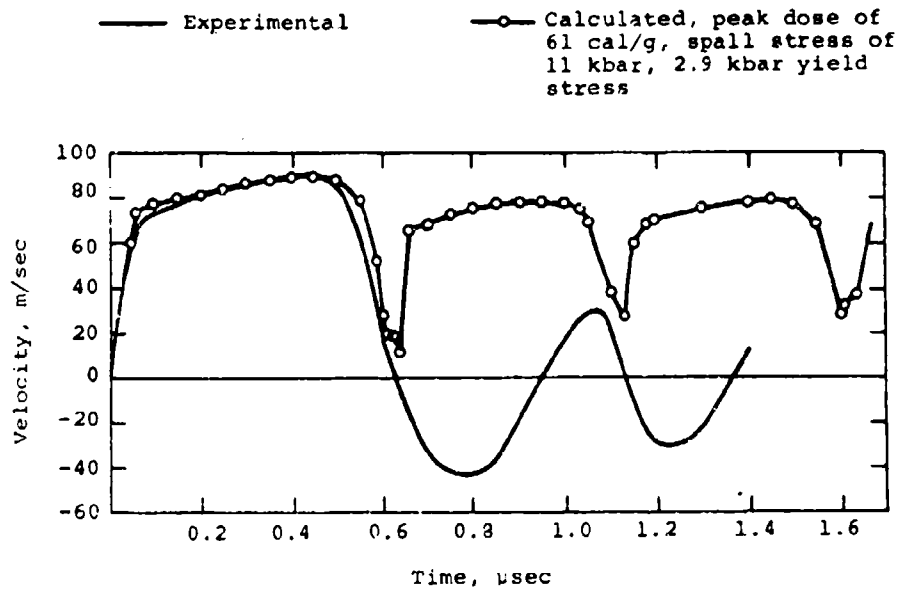


Figure 4.23 Comparison of measured and predicted response of 6061-T6 aluminum, shot no. 13080.

greater than one millimeter), which, based on the earlier data, would be expected for the estimated peak dose of 61 cal/g. Sample number 13091 exhibited no damage. From the free surface velocity, the peak dose is estimated as 39 cal/g, which is above the incipient spall threshold obtained on the PREDIX baseline material (cf. Figure 4.3). However, the material used in the interferometer experiments was not PREDIX stock, and the higher threshold is not inconsistent with observed batch-to-batch variations in the spall strength 6061-T6 aluminum reported here (Figure 4.13) and by Kreer (Reference 7).

Some additional independent tests are currently being conducted to establish the uncertainties that may be associated with the calorimetric data.

SECTION 5
DISCUSSION

SECTION 5

DISCUSSION

Computations of stresses required to produce incipient damage show that spall thresholds obtained using pulsed electron beams are substantially lower than those obtained in plate impact experiments (Reference 8). This, of course, immediately raises the question of the origin of the observed differences. Some possible causes are considered in the following discussion.

The possibility of a systematic error in the calorimetric measurements has been carefully considered. Unfortunately, in-situ calibration is difficult, especially for the intense <4.5 MeV> pulsed electron beams used in this work. A test was performed to determine the dose for the onset of melting in a tin slab, using essentially the same configuration as was employed in the spall experiments. The threshold dose to produce melting computed from the energy deposition profile and transmission calorimetry was within 10 percent of the handbook melt enthalpy. In other experiments, thermocouples on thin aluminum samples in the spall configuration gave results that agreed well with the dose levels computed from the transmitted fluences (Reference 9).

On the other hand, two points must be considered: (1) the lack of an absolute calibration of the voltage monitor and (2) the magnitude of the discrepancy between the computed dose levels and the measured free surface velocities in the laser interferometer experiments. These factors suggest that the question is not completely resolved, despite the stated shortcomings of the calorimetry used in the laser interferometer experiments.

Further insight into the bounds of the calorimeter's accuracy can be obtained by considering the results obtained in the electron beam experiments on preheated aluminum.

The melting range of 6061-T6 aluminum (Reference 1) lies between 580 and 650 C (1080 to 1200 F). For samples preheated to 400 F, an additional 68 cal/g of absorbed dose would be required to produce incipient melt. Referring to Figure 4.14, data were obtained on material preheated to 400 F for measured dose levels up to the order of 50 cal/g. Hence, assuming incipient melt could be observed in a photomicrograph of preheated material that received a peak dose of 70 cal/g (final temperature of 1100 F), the peak measured value of 50 cal/g could not be in error by as much as 20 cal/g, equivalent to a factor of 40 percent.

The effects of precompression represent another potential explanation for the different spall thresholds obtained in the two configurations. Shock precompression is present in plate impact, but not in pulsed electron beam experiments using uniform heating or in cases where front surface spall is considered. The results of work performed to date, while not definitive, have, however, tended to eliminate precompression as the source of the difference.

In the study of precompression effects, a rear surface spall threshold was obtained for stress pulses produced by deposition of <1 MeV> electrons in a 6061-T6 aluminum target that was thicker than the range of the electrons (Appendix D). In such a case, if there is no front surface spall, a tensile stress pulse follows the compressive stress pulse and superimposes with the reflected compressive pulse near the rear

surface. Thus, a given peak tension is produced in the material with roughly half the precompression as that required to produce the same peak tension using plate impact techniques. The incipient spall threshold thus obtained agreed with the plate impact data to within the experimental uncertainties.

ETI has reported (Reference 10) exploding foil data in which 6061-T6 aluminum targets were backed with a lower impedance material (magnesium and Lucite). In such a case, the precompression to achieve a given tensile stress is increased above that required when the rear surface of the aluminum is free. They concluded that an increase in precompression above that obtained in the usual plate impact experiments does not greatly change the stress-time conditions at the spall threshold.

The effects of shock precompression were further investigated by irradiating samples that had been subjected to compressive loading at ETI. The results of these experiments, described in Section 4, imply that the effects of precompression, if present, are too small to account for the difference between electron beam and gas gun data. However, several factors could account for the failure to demonstrate an appreciable difference from the experiments on virgin material. First, the length of time between the shock compression of the samples and their exposure in the pulsed electron beam was on the order of a day or longer. During this time, recovery processes could relieve localized residual stress concentrations. In addition, Jones (Reference 11) has shown that lateral stress relief after shock precompression has a considerable effect upon the strain history of the material. Hence, at the time that spall occurs, precompressed samples that have undergone lateral stress relief are not truly representative of material subjected only to plate impact or the

pulsed electron beam where the entire response consists of uniaxial strain up to spall. This detailed strain-loading history may be quite important if the differences in the two configurations are associated with the Bauschinger effect.

Other phenomena may account for observed differences in the spall thresholds; differences exist in the detailed loading history of the material at the spall plane in the two configurations. The difference in the stress histories obtained in electron beam and plate experiments are illustrated in Figure 5.1, where the axial stress (the component of stress in

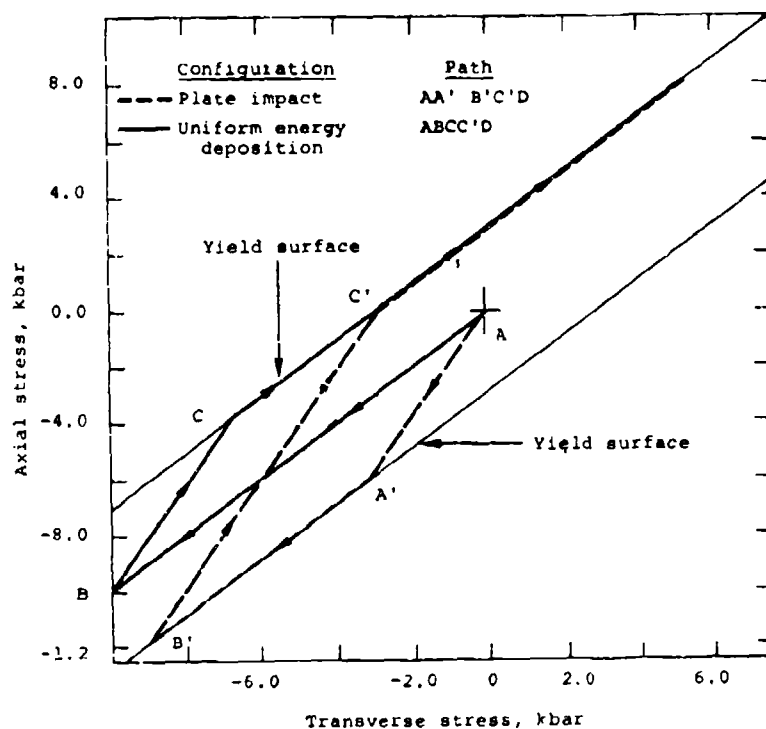


Figure 5.1 Axial versus transverse stress paths at the spall plane in plate impact and electron beam experiments.

the direction of the wave propagation) is shown as a function of the transverse stress. In plate impact, the initial loading occurs elastically with $d\sigma_T = \nu/(1-\nu) d\sigma_A$ (where ν is Poisson's ratio) along A-A', until the yield surface is reached at A'. Additional loading produces yielding and each subsequent increment in axial stress is matched by an equal increment of transverse stress. After the plastic compression A'-B', the material remains in the compressed state B' until the trailing rarefaction and reflection tension lead first to elastic unloading B'-C', and then plastic unloading to the tensile state D where fracture may or may not occur.

In the electron beam case, on the other hand, as energy is deposited pressure is generated and the initial loading is hydrostatic from A to B; this occurs at nearly constant volume, so there is no compression or shear. The material remains in this state, B, until the arrival of rarefaction waves from the free surfaces; then it unloads, first elastically along B to C and then plastically along C to D to the tensile state D.

This illustrates two significant differences between plate impact and electron beam loadings. First, less plastic work is produced in the electron beam loading; second, the direction of shear stress reverses for plate impact, but not in the case of the electron beam. Consequently, there can be no Bauschinger effect in the latter case.

It can also be seen from Figure 5.1 that the stress state in tension for the two cases is the same, provided work hardening is not significant.

Tuler (Reference 9) compared the computed strains at the spall threshold for the plate impact and electron beam data and found a rather dramatic correlation. On this basis, he has suggested that a critical strain criterion, rather than a critical stress criterion, may be appropriate.

The sequence of stress states during tensile loading up to failure are, as noted above, the same for the two types of experiments. Hence, at the time that axial stress goes into tension (aside from the total amount of plastic work), the material states for the same tensile stress value for plate impact and electron beam experiments differ primarily in axial strain, density, and temperature. In plate impact experiments for 6061-T6 aluminum, targets were heated to initial temperatures comparable to those produced by the electron energy depositions; however, too small a drop in the spall threshold was observed to ascribe the differences in stress to temperature alone. Consequently, the strain difference (for a given tensile stress) appears to provide a likely explanation.

Close examination of the critical strain criterion, however, raises some fundamental questions concerning its physical basis. The data for 6061-T6 aluminum presented by Tuler are shown replotted in Figure 5.2, but in the form of axial stress versus density (normalized to its room temperature, atmospheric pressure value) at the plane of peak tension. Also shown are loading-unloading paths for material preheated to 170 C and subjected to plate impact loading at several impact velocities.

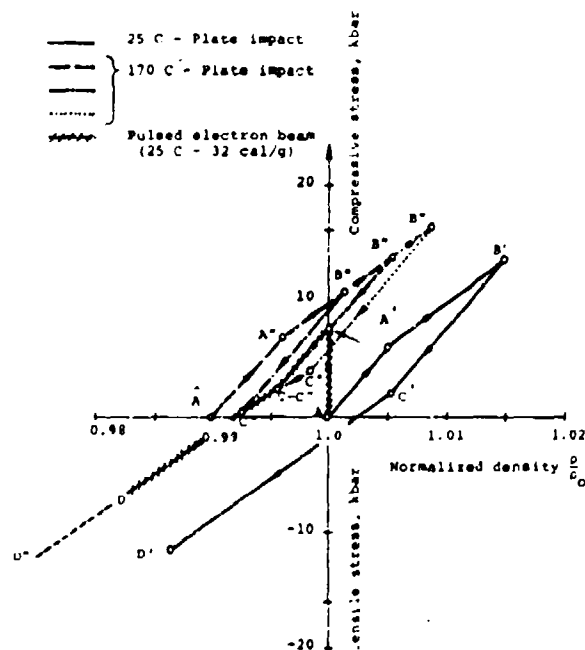


Figure 5.2 Dynamic loading paths for 6061-T6 aluminum in pulsed electron beam and plate impact experiments.

The sequence of states for the electron beam irradiated material is denoted by A-B (hydrostatic loading), B-C (elastic unloading), and C-D (plastic unloading). For the room temperature plate impact case, the sequence is A-A' (elastic loading), A'-B' (plastic loading), B'-C' (elastic unloading), and C'-D' (plastic unloading). The sequence of states for the preheated material subjected to plate impact is $\hat{A} - A'' - B'' - C'' - D''$.

By selection of the proper preheating temperature, the plastic unloading path (C''-D'') for the plate impact can be made to coincide with the plastic unloading path (C-D) for the pulsed electron beam irradiated material. Hence, the sequence of axial stress versus density states leading up to incipient spall formation are the same. Moreover, the stress deviators (i.e., the differences between the transverse and axial stresses) are

also the same at tensile stress levels where plastic unloading is occurring for both types of experiments.

Finally, the strain deviators are also the same. This can be shown as follows.

The strain deviators are defined as

$$\theta_A = \epsilon_A - \theta$$

$$\theta_T = \epsilon_T - \theta$$

where

$$\theta \equiv 1/3 (\epsilon_A + 2 \epsilon_T)$$

Since $\epsilon_T \equiv 0$,

$$\theta_A = 2/3 \epsilon_A = 2/3 \left(\frac{\rho}{\rho_0} - 1 \right)$$

$$\theta_T = -1/3 \epsilon_A = -1/3 \left(\frac{\rho}{\rho_0} - 1 \right)$$

Consequently, the strain deviators are directly related to the density. Thus, if axial stress versus density states are matched during the plastic unloading prior to spall, the material states (i.e., all the stress and strain components) are equivalent near the failure point for both electron beam and heated plate impact experiments.

Another way to view the critical strain hypothesis is to consider the appropriate reference state. For the electron beam

case, the reference state should not be the material at its original density, that is, the state prior to irradiation. Rather, the strain in the irradiated material should be referenced to its stress free state. This is shown by considering that the material state obtained by constant volume heating could also be obtained by heating at zero pressure (free expansion), which does not induce any strain, and then by compressing the material hydrostatically back to its original volume. This imposes a net elastic strain, and is equivalent to the state following sudden energy deposition. When this elastic strain is considered, there is no longer a correlation between the maximum strains obtained for the plate impact and pulsed electron beam experiments.

Looking further for potential explanations of the observed differences, one factor is the time at temperature. The pre-heated plate impact samples are at or near the final temperature for a long time (several minutes) compared to the electron beam samples which undergo tensile loading after times at temperature on the order of a microsecond or less. Data (Reference 9) on the temperature induced degradation of the yield strength of 6061-T6 aluminum for short times at temperature following submicrosecond heating ($\sim 200 \mu\text{sec}$ to 10 msec) indicate that the extent of strength degradation is appreciably less than for longer times at temperature. These data are shown in Figure 5.3; they indicate that the yield strength in the high temperature plate impact shots (and the pre-heated target electron beam shots) were significantly lower. This lower yield strength may imply an increase in ductility. As a result, the plastic shear strains may be less likely to produce void nucleation sites, and once voids are formed, the ductility will require greater stresses to propagate cracks. This is attributed to extensive plastic

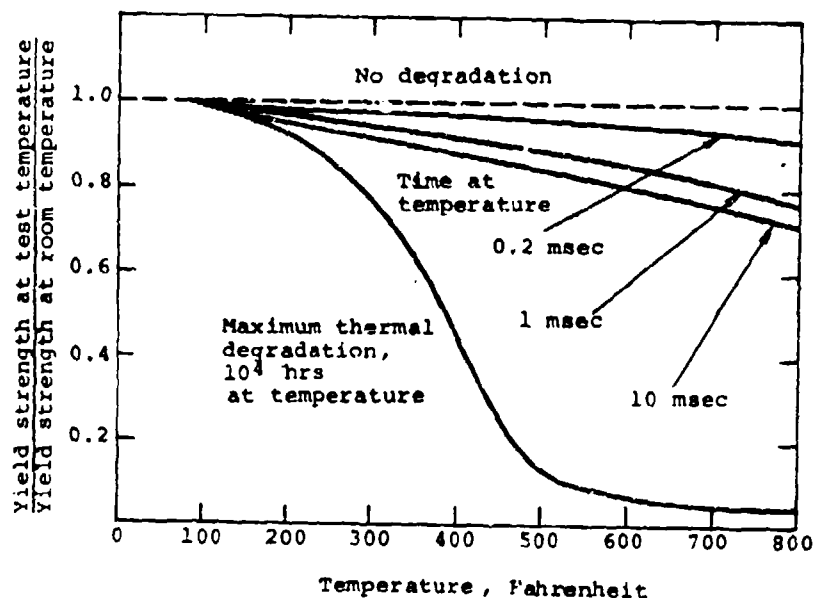


Figure 5.3 Thermal degradation of the yield strength for 6061-T6 aluminum following instantaneous heating.

deformation which blunts the tips of moving cracks, thereby increasing the stress required for further crack growth. Thus, the effect of decreases in yield strength at the elevated temperatures upon the spall threshold may be compensated by the concomitant increase in ductility. In the case of the electron beam irradiations (without long soak time preheating), the material with higher yield stress may tend to behave in a less ductile fashion. Admittedly, a correlation between yield strength and spall strength is not obvious, nevertheless, the trends shown by both the pre-heated flier plate and electron beam data are consistent with the above explanation.

Plastic shear strains have been shown to create void nucleation sites in tests in which failure occurred at lower tensile stresses if preceded by torsional plastic shear (Reference 12). It should be noted that by reversing the plastic

shear strain before applying tension restored some of the tensile strength. Thus, the reversal of the shear strains that occurs in the plate impact experiments may also be related to its apparent greater tensile strength.

One additional possible explanation is that differences result from the radiation damage induced by the high energy electrons. A reasonable value for the fractional number of atom displacements, F , can be obtained from the relationship (Reference 13)

$$F = n (2.5 \times 10^{-25}) z^2 \frac{(1-\beta^2)}{\beta^4} \left\{ (y-1) - \beta^2 \ln y + 0.023 z \beta \left[2(y^{1/2}-1) - \ln y \right] \right\}$$

where

$$y \approx \left(\frac{4 m_0}{M} \right)^2 \frac{E}{\epsilon_0} \left(1 + \frac{E}{2 m_0 c^2} \right)$$

E = the electron energy

ϵ_0 = the threshold displacement energy (~ 25 eV)

m_0 = the electron rest mass

M = the target atomic mass

z = the target atomic number

c = the velocity of light

$\beta = \frac{v}{c}$, the ratio of electron velocity to c

n = the number of electrons incident/cm²

To produce a dose of 30 cal/g, a flux of 4×10^{14} electrons/cm² of 4 MeV electrons is required. In aluminum this produces roughly one primary atomic displacement in every 10^9 atoms. This is an order of magnitude lower than can be detected by changes

in mechanical properties (Reference 14). The energy of the electrons is large compared to the threshold energy to produce atomic displacements (~ 0.5 MeV), so multiple atom displacements are probably likely. However, the low density of primary displacements suggests that the defects produced by the beam are not likely to materially affect mechanical properties.

In addition, radiation-damage data on aluminum alloys (Reference 13) obtained with neutrons ($\sim 10^{20}/\text{cm}^2$) had the effect of increasing both yield and ultimate tensile strengths.

SECTION 6
CONCLUSIONS

SECTION 6

CONCLUSIONS

Techniques have been developed to determine thresholds for spall produced by sudden, uniform volume heating of materials. The threshold dose values to produce incipient and complete spall have been measured as a function of sample thickness (i.e., pulse duration) for 6061-T6 aluminum, alpha titanium, and OFHC copper.

The data predict a lower peak tensile stress to produce damage than is computed from data obtained in plate-impact experiments for equivalent tensile pulse durations. This observed difference is greater than can be attributed to differences in definition of spall damage levels, scatter in material properties, heating rate, temperature and time at temperature effects, and estimated experimental uncertainties.

Several potential explanations for this difference have been suggested. However, no single explanation is clearly satisfactory either because of insufficient experimental verification or the lack of a sound physical basis.

At present, the most likely explanation appears to be related to either (1) the Bauschinger effect or an integral over the plastic strain, or (2) a systematic discrepancy in the calorimetric measurements used in the electron beam experiments.

A definitive resolution of the observed differences in dynamic fracture thresholds induced by plate impact and rapid heating must wait a thorough examination of calorimetric techniques and further actively instrumented, uniform heating experiments.

REFERENCES

1. RADS Handbook, Vol. 10, AVCO Corporation (1969).
2. B. Alder et al, Methods in Computational Physics, Vol. 1, Academic Press, New York, N. Y., 1963.
3. R. Parker, "Rapid Phase Transformation in Titanium Induced by Pulse Heating," Trans. AIME, 233, 1545 (1965).
4. L. M. Barker and R. E. Hollenbach, Rev. Sci. Instr. 36, 1617 (1965).
5. L. M. Barker, "Fine Structure of Compressive and Release Wave Shape in Aluminum Measured by the Velocity Interferometer Technique," IUTAM Symposium HDP, Paris (September 1967).
6. W. Isbell et al., "Measurements of Dynamic Properties - Results for Metals," General Motors Materials and Structures Laboratory (to be published as DASA-2501-3, -4, -5, and -6 in June 1971).
7. J. R. Kreer, "Dynamic Fracture in 6061-T6 Aluminum," AFWL-TR-70-180, Air Force Weapons Laboratory (January 1971).
8. F. R. Tuler, "Tensile Strain as a Criterion for Spallation in Metals," Proceedings of the 17th Sagamore Conference (September 1970), in press.
9. T. Stefansky et al., "Tensile Properties Experiments," PIFR-211, Physics International Company, San Leandro, California, in preparation.
10. D. V. Keller and F. R. Tuler, "Predix Metals Report," Preliminary Draft, CR 70-06, Effects Technology, Inc., Santa Barbara, California.

REFERENCES (cont.)

11. O. E. Jones and A. L. Stevens, "Effects of Radial Release Waves in Plate Impact Experiments," Bull. Am. Phys. Soc., 15, 1606 (1970).
12. D. McLean, Mechanical Properties of Metals, John Wiley and Sons, Inc., New York, N. Y. (1962), p. 234.
13. J. P. Howe and S. Siegel, "Radiation Damage to Solids," Nuclear Engineering Handbook, H. Etherington, ed., McGraw-Hill Book Company, Inc., New York, N. Y., (1958), p. 10-83.
14. J. W. Corbett, Electron Radiation Damage in Semiconductors and Metals, Solid State Physics, Supplement 7, Academic Press, New York, N. Y. (1966).

APPENDIX A

DEPOSITION PROFILES AND INCIDENT FLUENCES FOR
THE SHOTS NEAREST TO THE SPALL THRESHOLDS IN
6061-T6 ALUMINUM INITIALLY AT ROOM TEMPERATURE

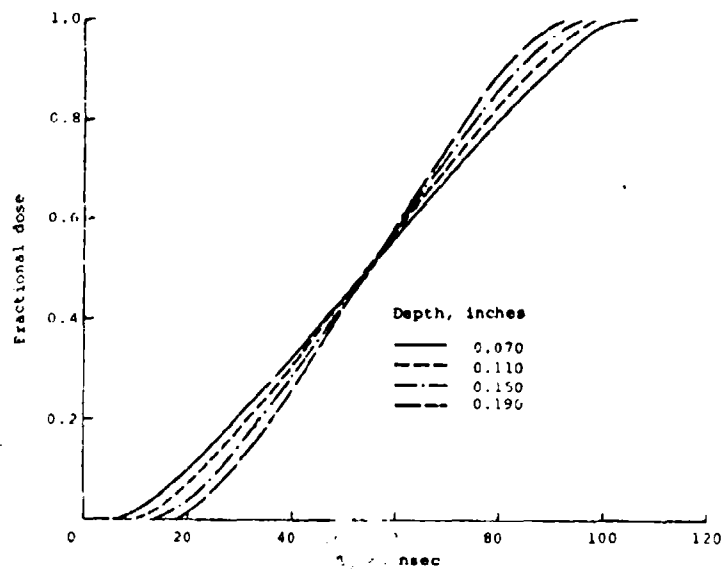


Figure A.1 Time dependence of energy deposition in aluminum for a typical 1140 Pulserad <4.5> spectrum.

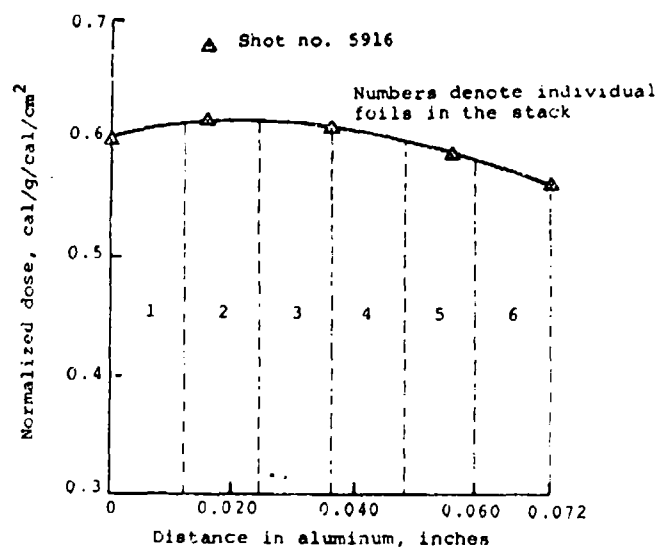


Figure A.2 Deposition profile for shot no. 5916 in 6061-T6 aluminum.

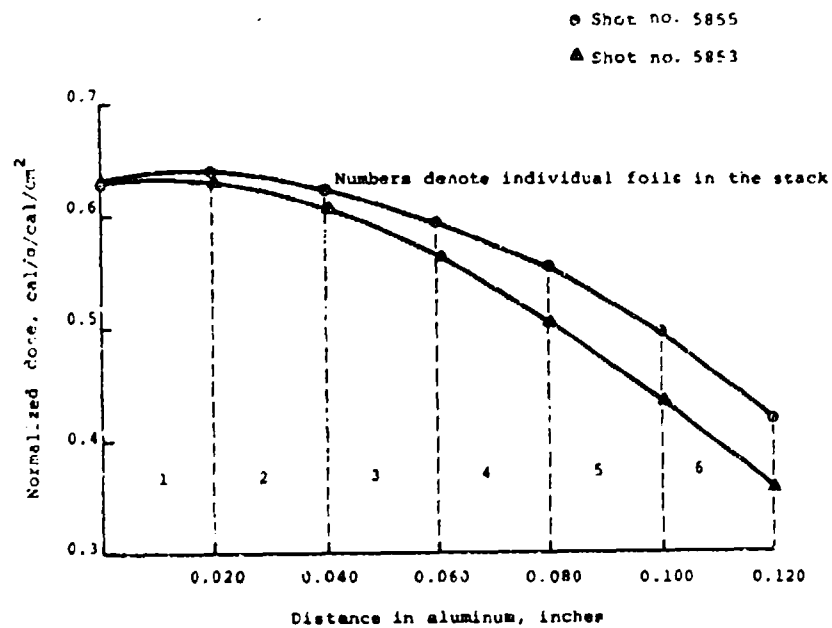


Figure A.3 Deposition profiles for shots no. 5855 and 5833 in 6061-T6 aluminum.

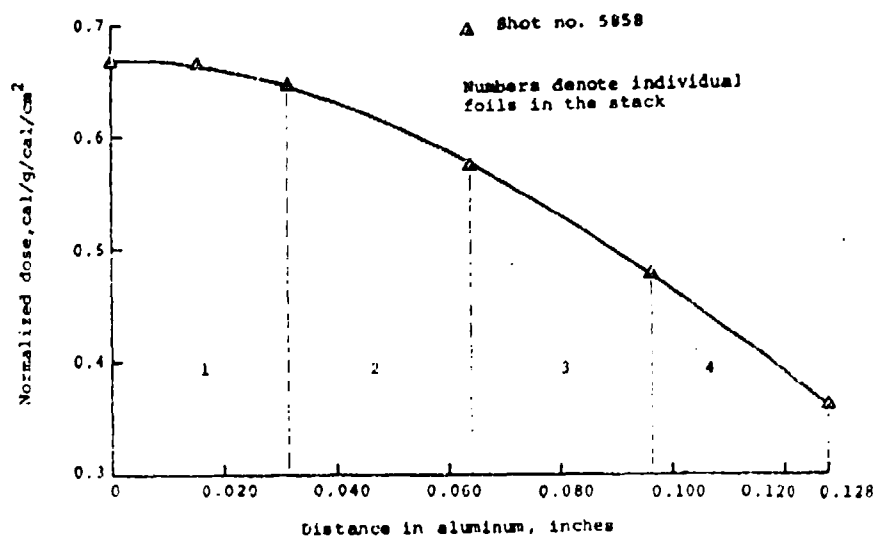


Figure A.4 Deposition profiles for shot no. 5858 in 6061-T6 aluminum.

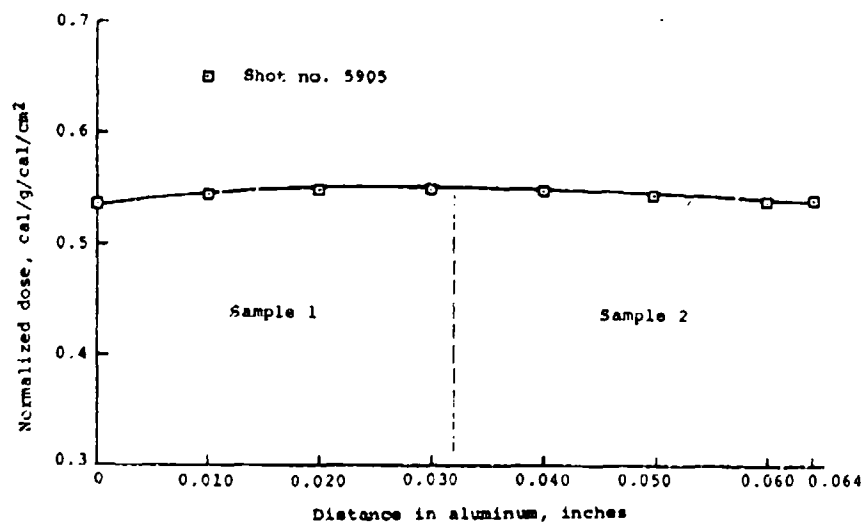


Figure A.5 Deposition profiles for shot no. 5905 in 6061-T6 aluminum.

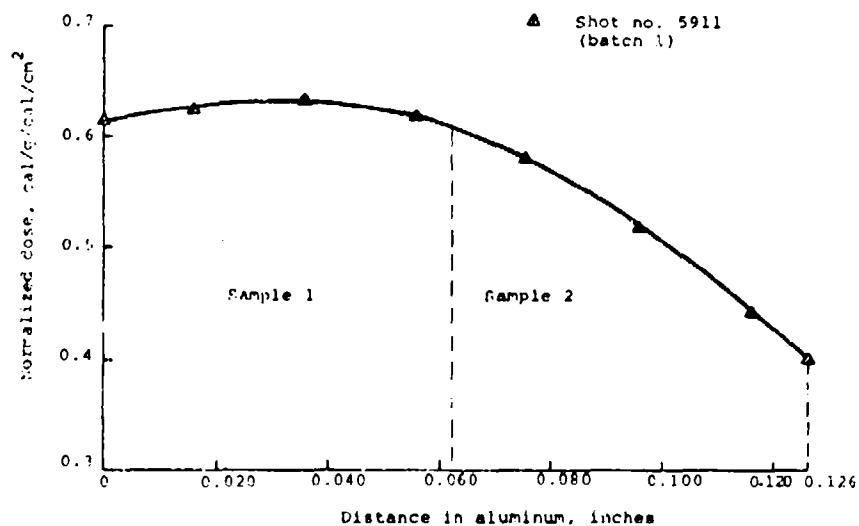


Figure A.6 Deposition profiles for shot no. 5911 in 6061-T6 aluminum.

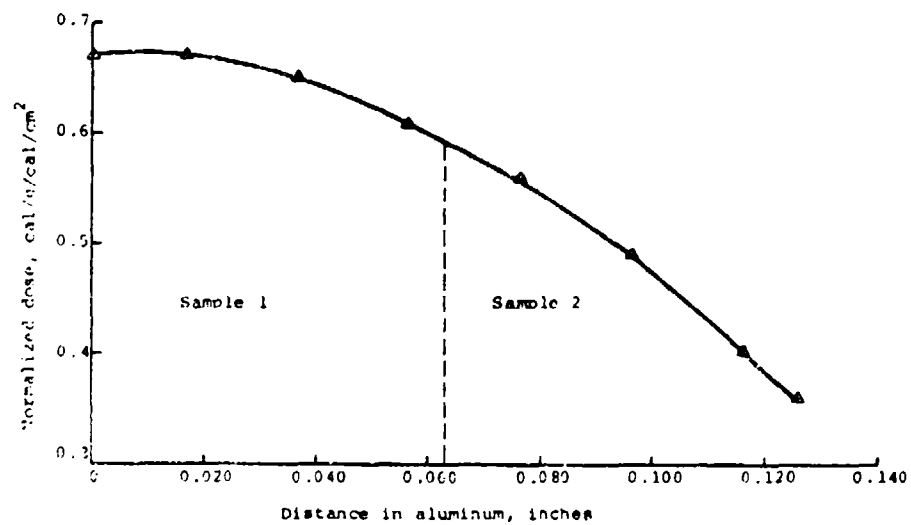


Figure A.7 Deposition profile for shot no. 5960 in aluminum.

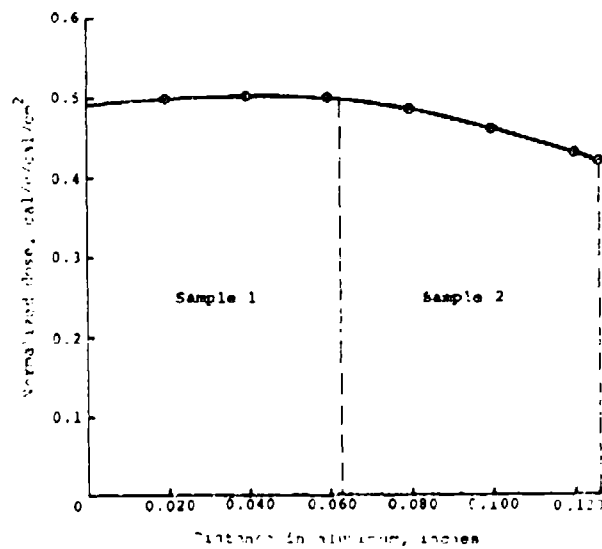


Figure A.8 Deposition profile for shot no. 8522 in aluminum.

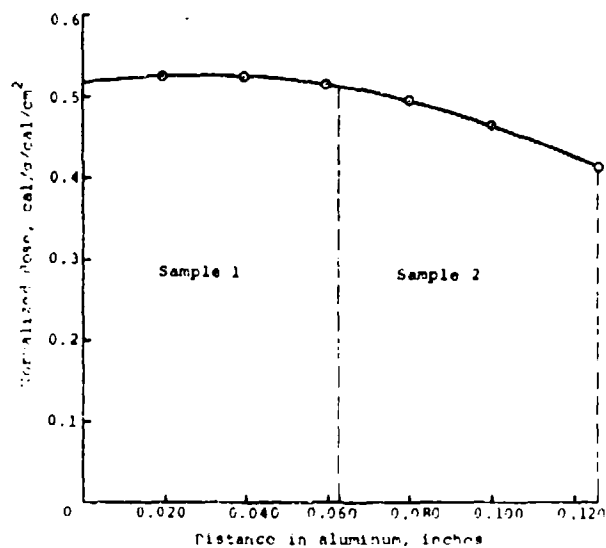


Figure A.9 Deposition profile for shot no. 8523 in 6061-T6 aluminum.

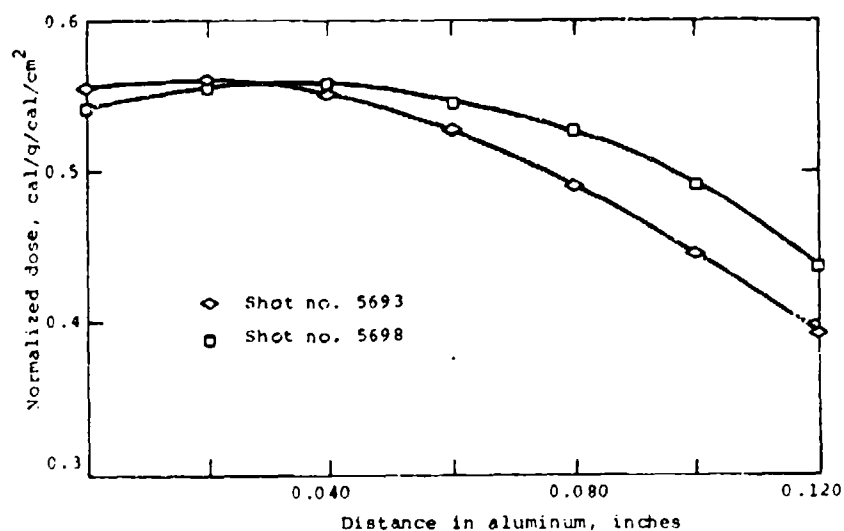


Figure A.10 Deposition profiles for shots no. 5693 and 5698 in aluminum.

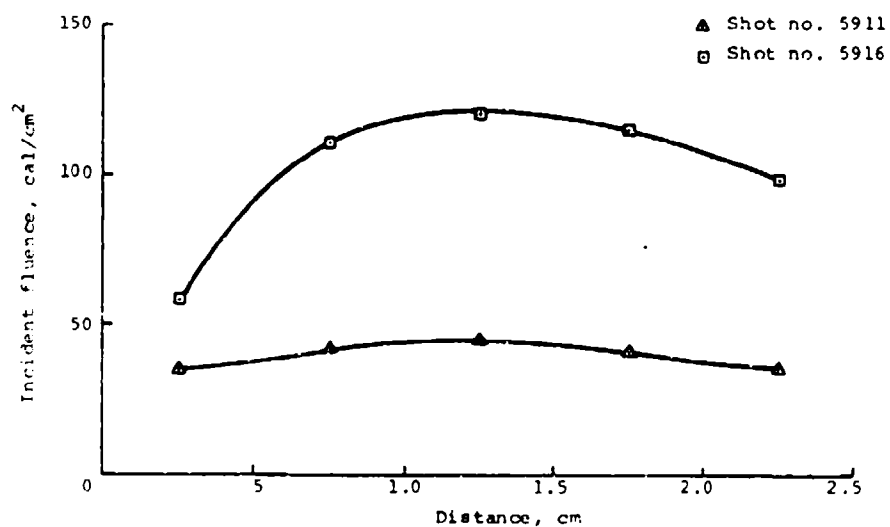


Figure A.11 Peak incident fluence profile for shots no. 5911 and 5916 in 6061-T6 aluminum.

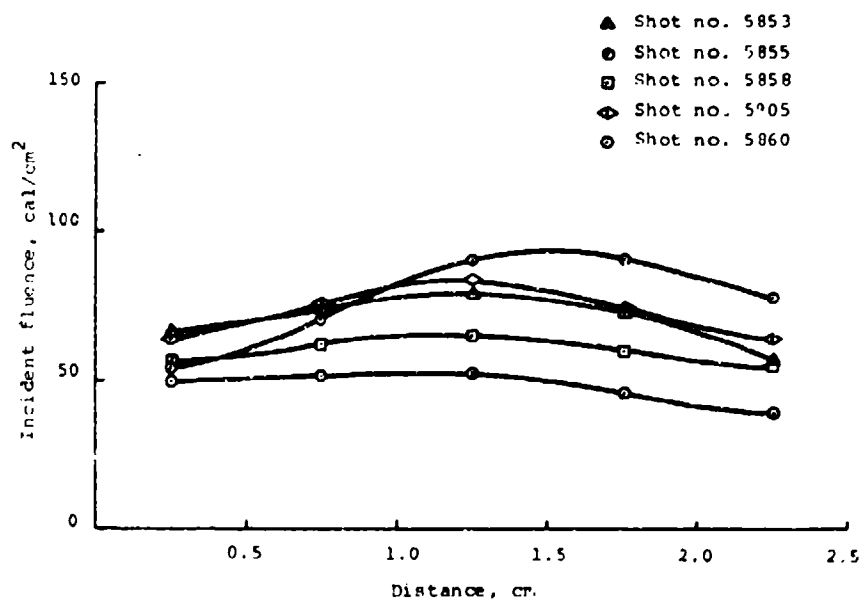


Figure A.12 Peak incident fluence profiles in 6061-T6 aluminum for shots no. 5853, 5855, 5858, 5905, and 5960.

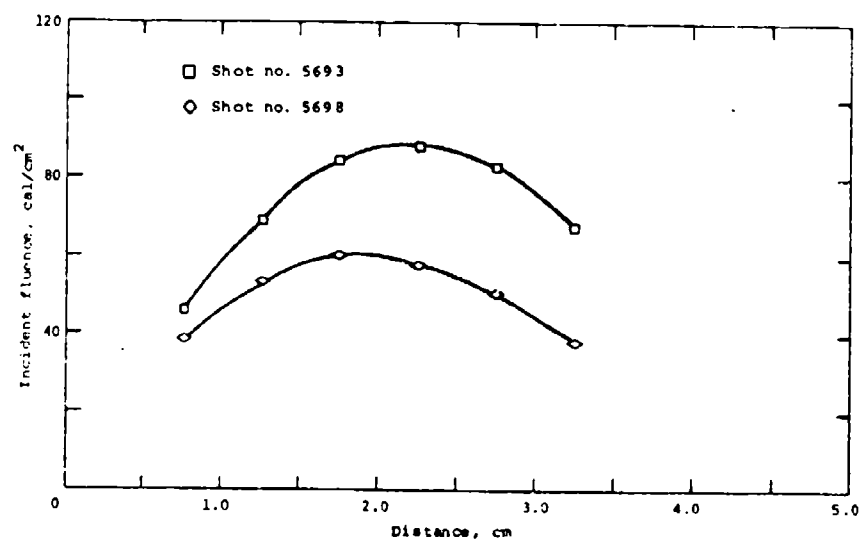


Figure A.13 Peak incident fluence profile for shots no. 5693 and 5698 in 6061-T6 aluminum.

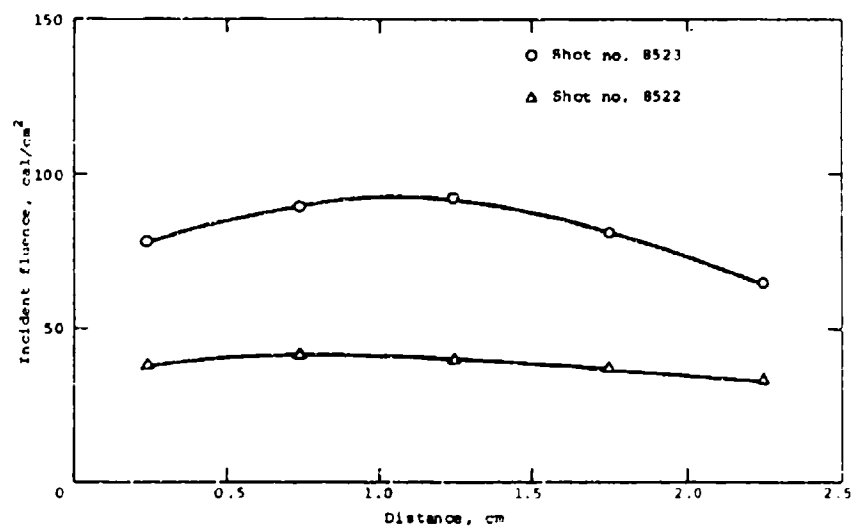


Figure A.14 Peak incident fluence profile for shots no. 8522 and 8523 in 6061-T6 aluminum.

APPENDIX B

DEPOSITION PROFILES AND INCIDENT FLUENCES FOR
THE SHOTS NEAREST TO THE SPALL THRESHOLDS IN
ALPHA TITANIUM INITIALLY AT ROOM TEMPERATURE

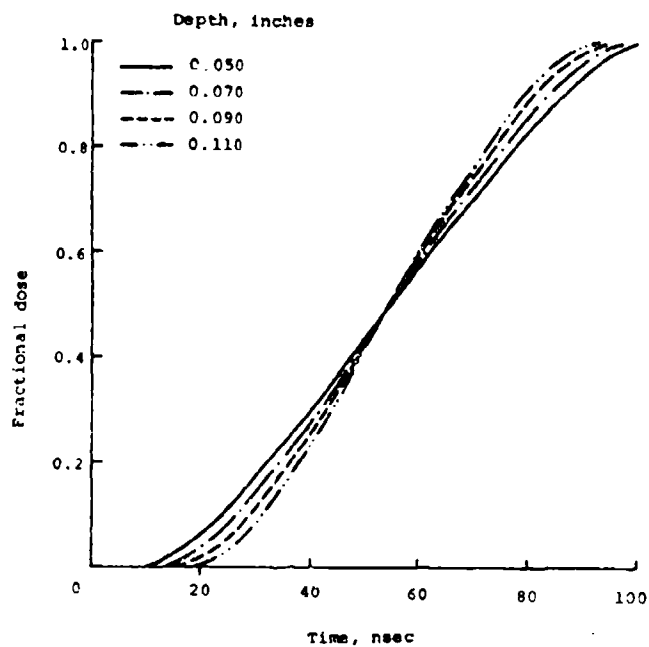


Figure B.1 Time dependence of energy deposition in titanium.

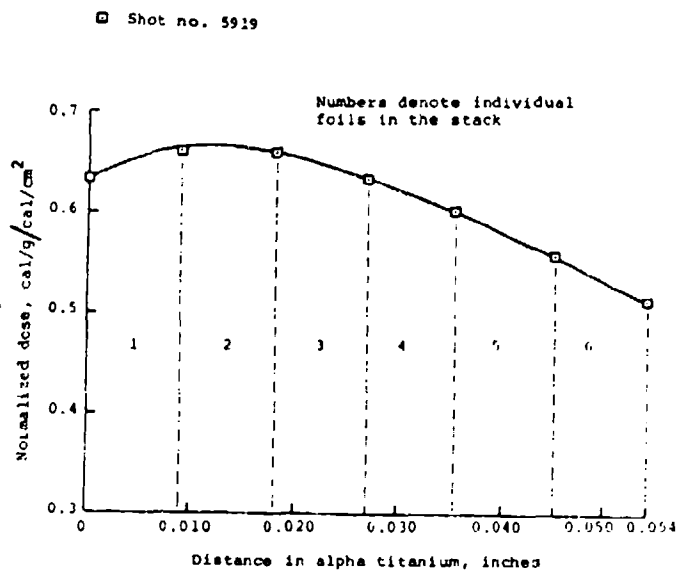


Figure B.2 Deposition profile for shot no. 5919 in alpha titanium.

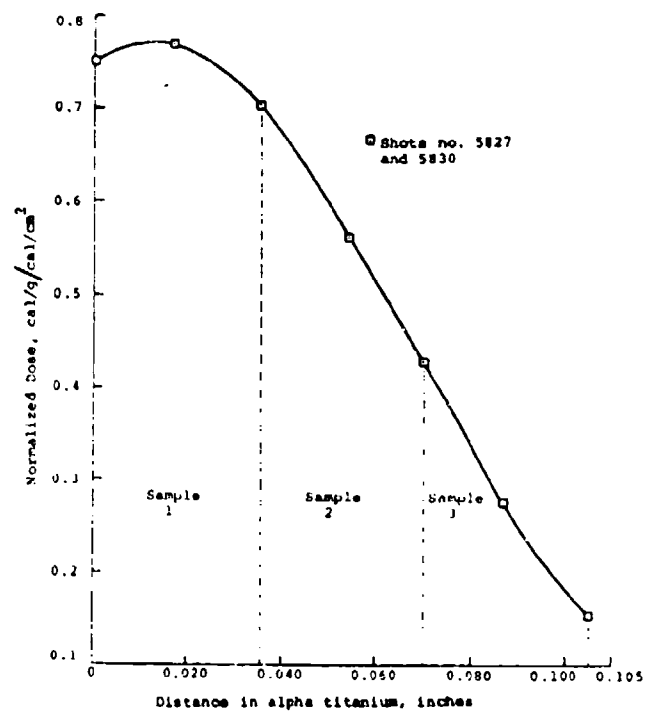


Figure B.3 Deposition profile for shots no. 5827 and 5830 in alpha titanium.

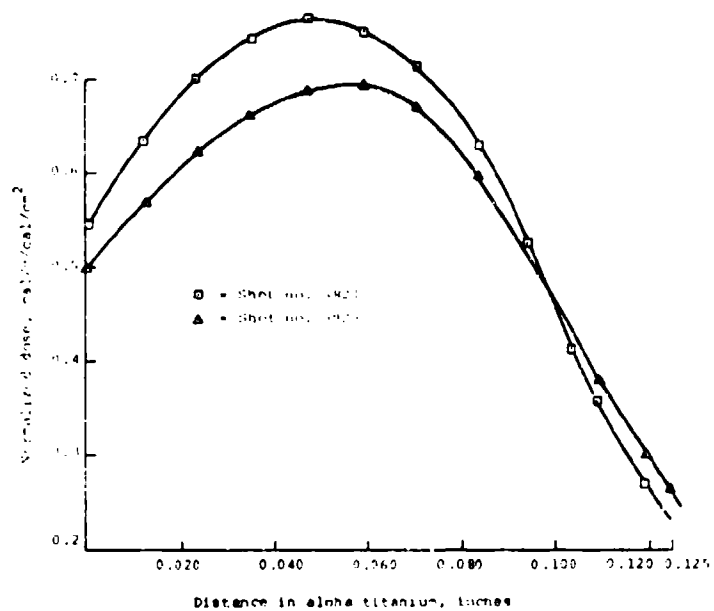


Figure B.4 Deposition profiles for shots no. 5821 and 5825 in alpha titanium.

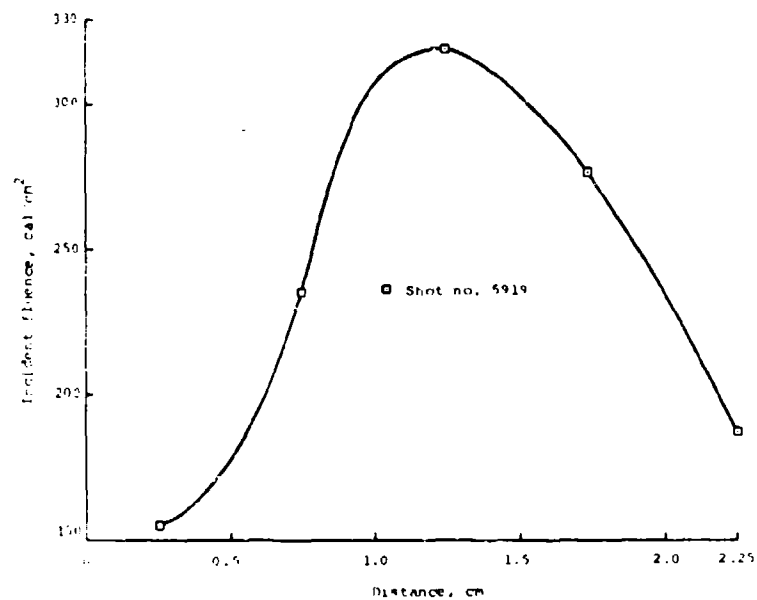


Figure B.5 Peak incident fluence profile for shot no. 5919 in alpha titanium.

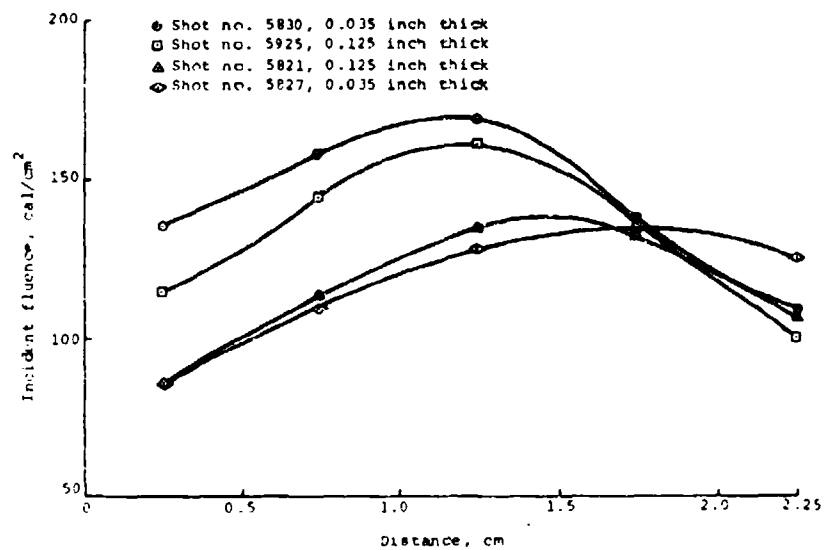


Figure B.6 Peak incident fluence profile for shots no. 5830, 5925, 5821, and 5827 in alpha titanium.

APPENDIX C

DEPOSITION PROFILES AND INCIDENT FLUENCES FOR THE
SHOTS NEAREST TO THE SPALL THRESHOLDS IN OFHC COPPER
BAR AND SHEET STOCK INITIALLY AT ROOM TEMPERATURE

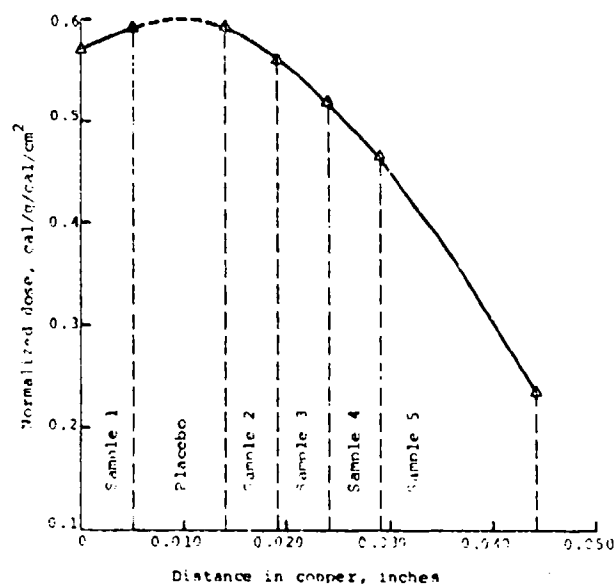


Figure C.3 Deposition profiles for shot no. 6770 in copper bar stock.

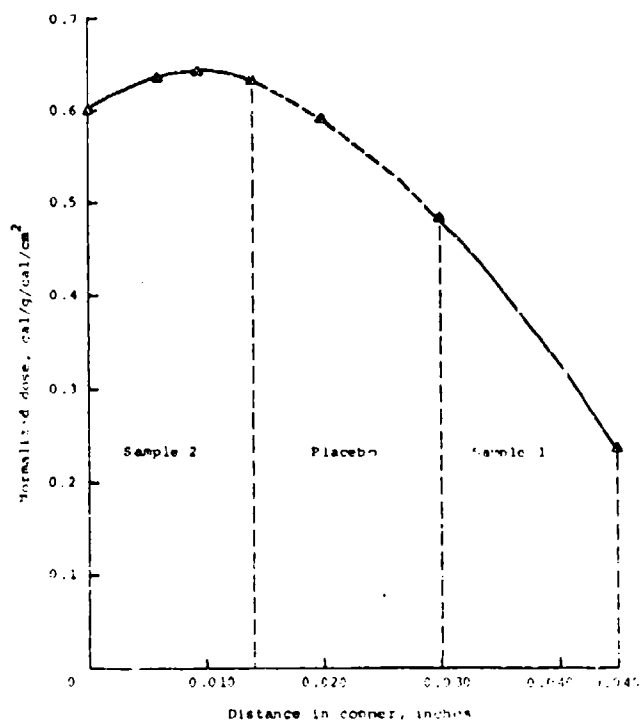


Figure C.4 Deposition profiles for shot no. 6292 in copper bar stock.

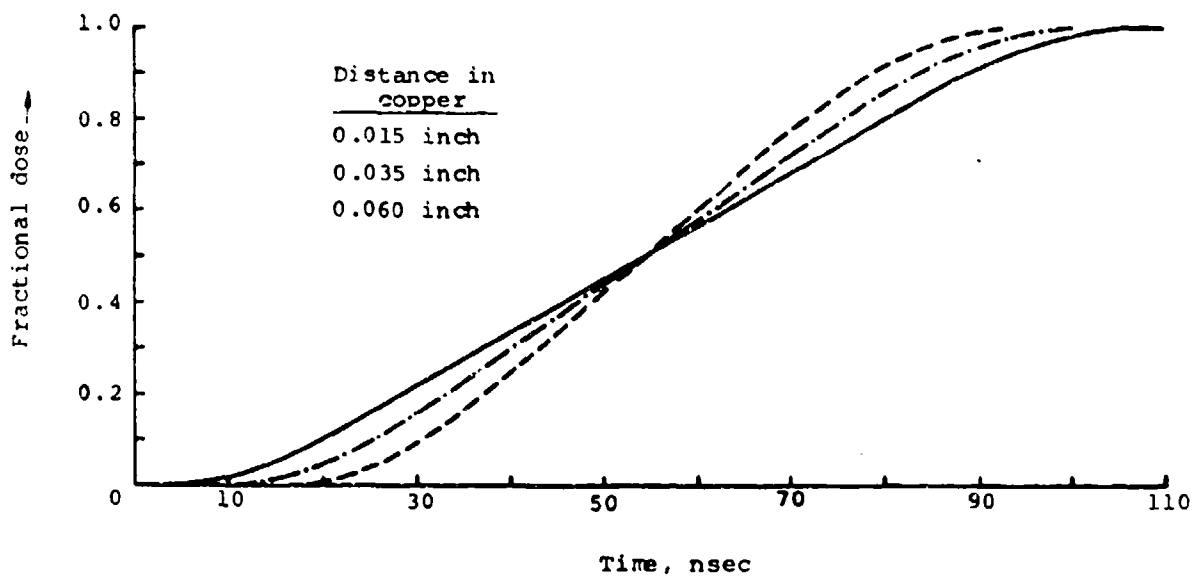


Figure C.1 Time dependence of energy deposition in OFHC copper for a typical 1140 Pulserad, 4.5-MeV mean electron energy spectrum.

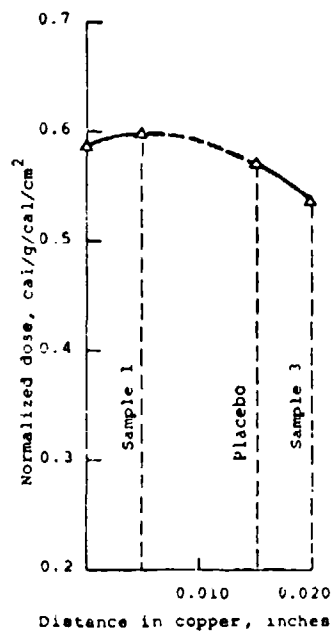


Figure C.2 Deposition profiles for shot no. 6781 in copper bar stock.

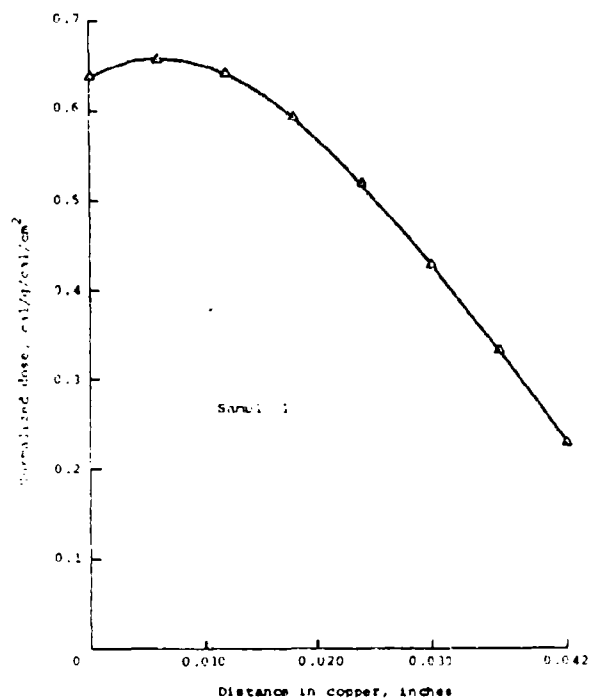


Figure C.5 Deposition profile for shot no. 6285 in copper bar stock.

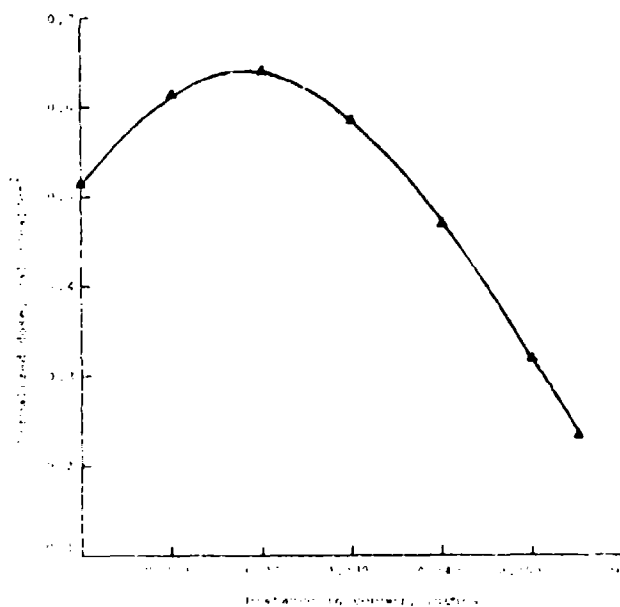


Figure C.6 Deposition profiles for shot no. 6287 in copper bar stock.

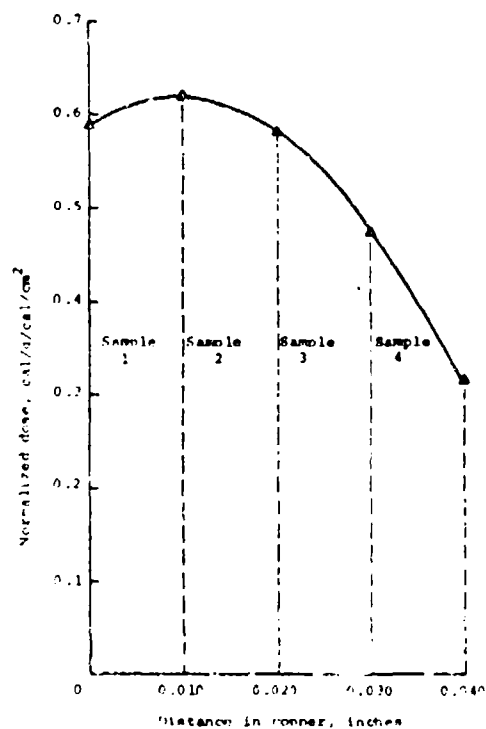


Figure C.7 Deposition profiles for shots no. 6534 and 6536 in copper sheet stock.

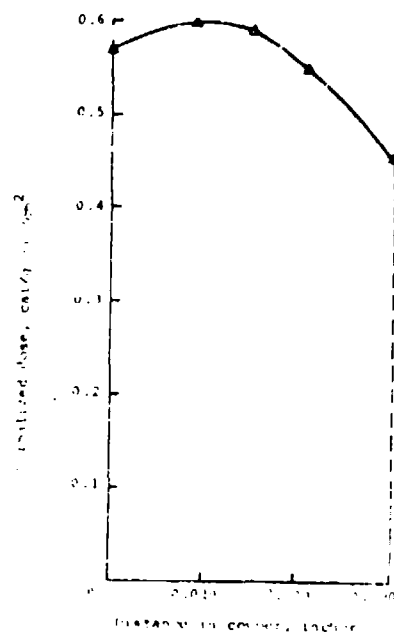


Figure C.8 Deposition profiles for shots no. 6530 and 6763 in copper sheet stock.

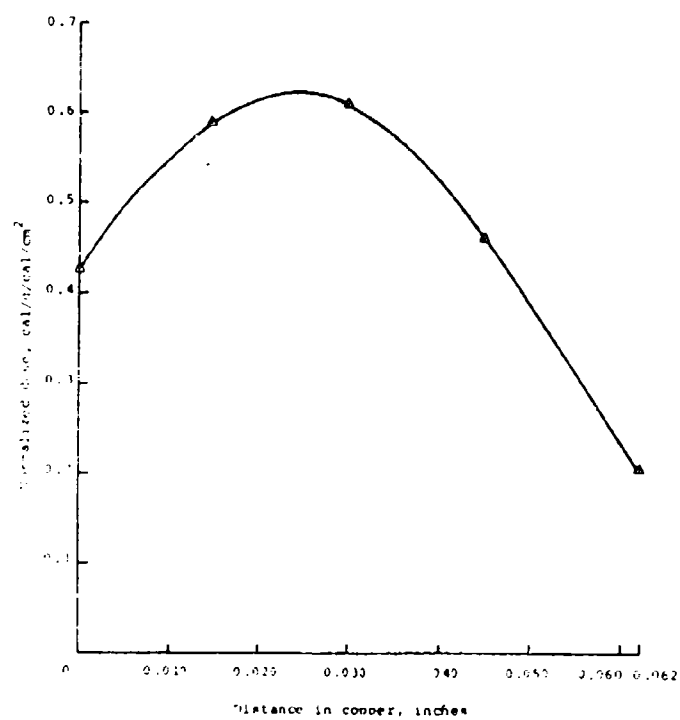


Figure C.9 Deposition profiles for shot no. 6524 in copper sheet stock.

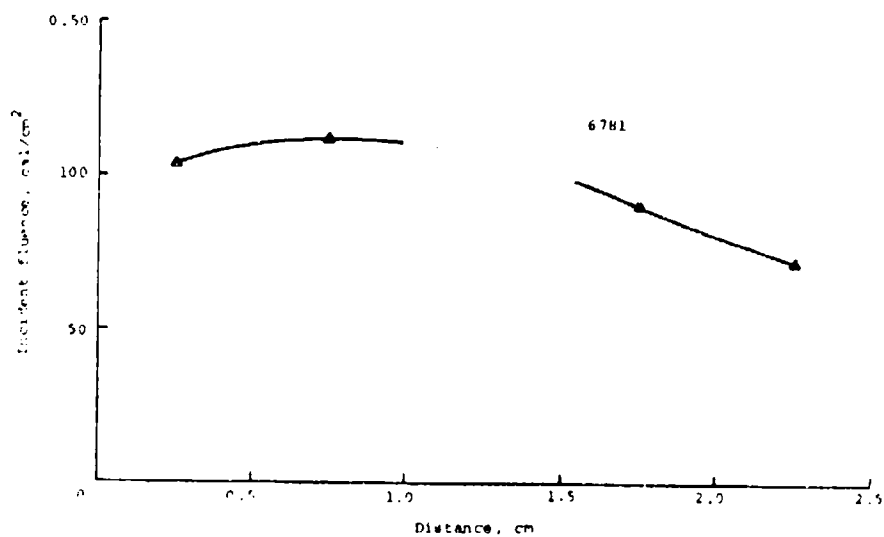


Figure C.10 Peak incident fluence profile for shot no. 6781 in copper bar stock.

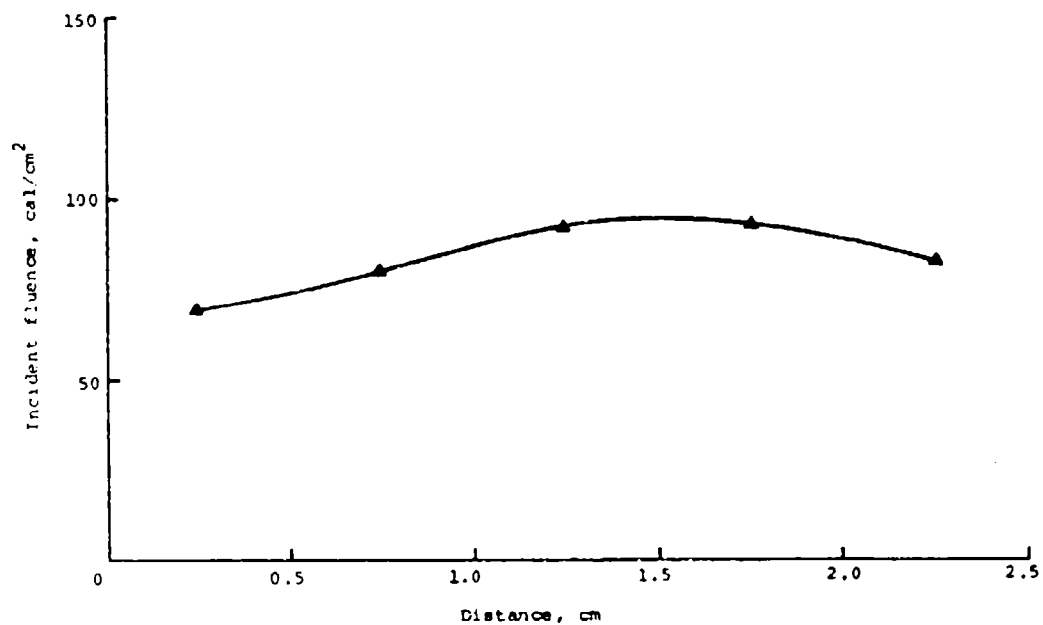


Figure C.11 Peak incident fluence profile for shot no. 6770 in copper bar stock.

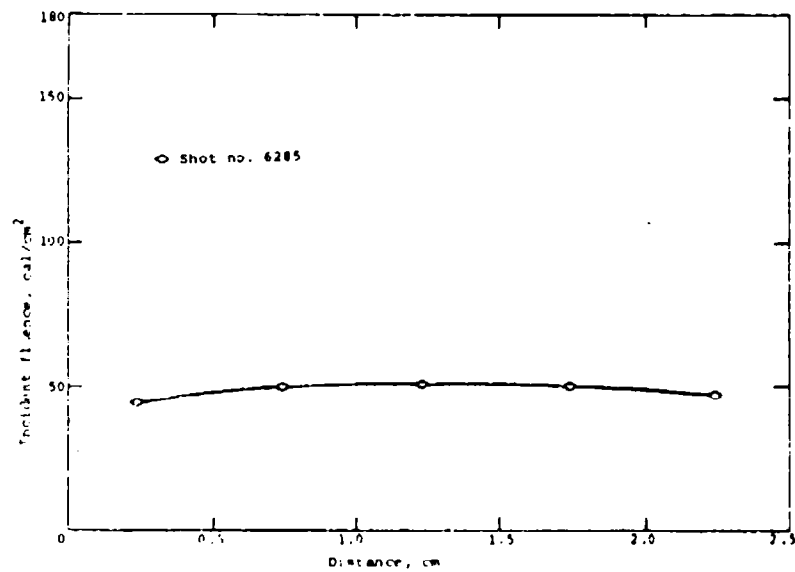


Figure C.12 Peak incident fluence profile for shot no. 6285 in copper bar stock.

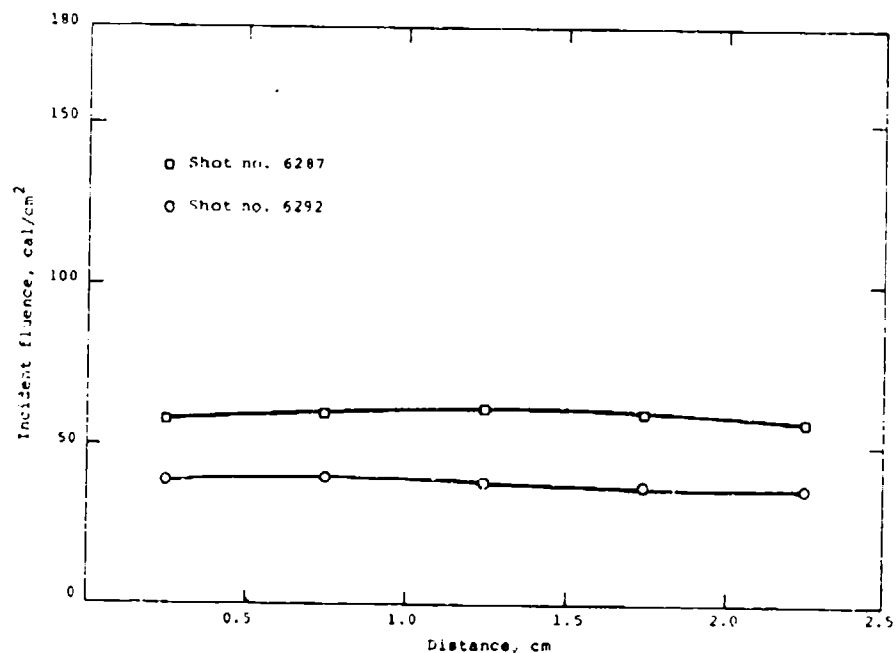


Figure C.13 Peak incident fluence profile for shots no. 6287 and 6292 in copper bar stock.

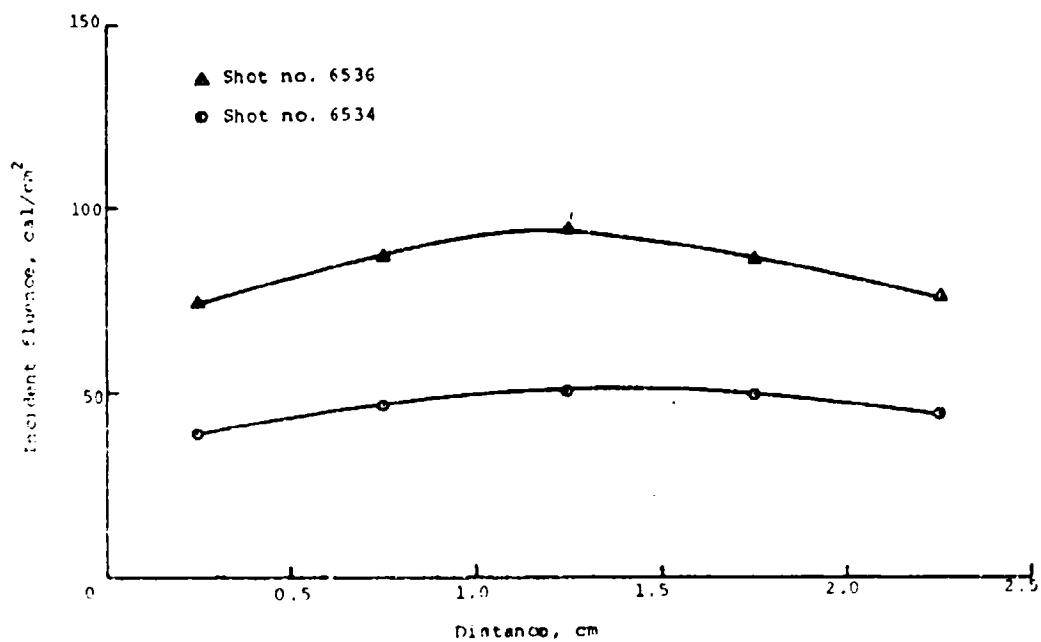


Figure C.14 Peak incident fluence profiles for shots. no. 6536 and 6534 in copper sheet stock.

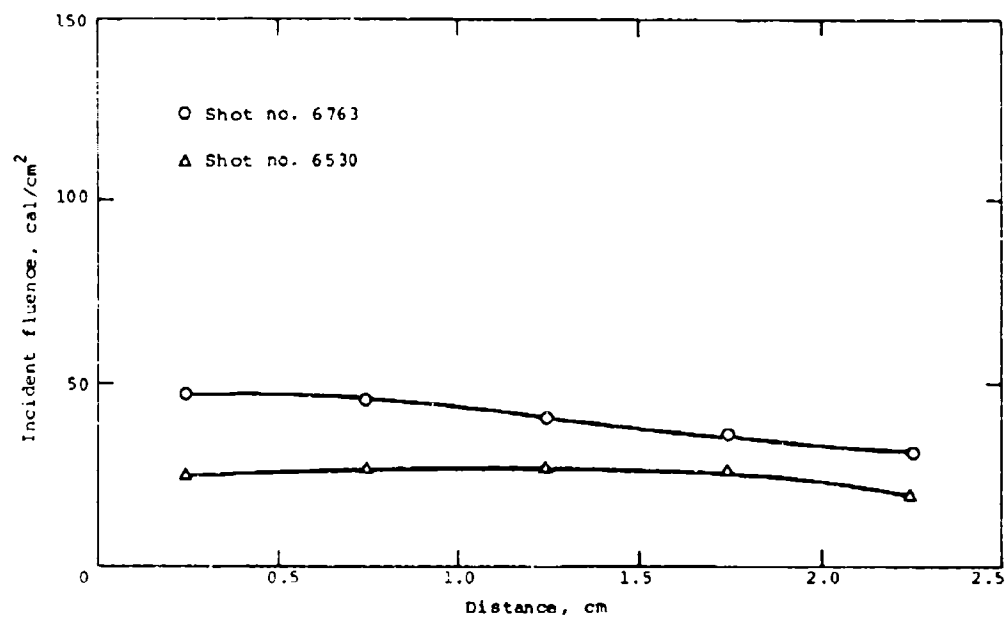


Figure C.15 Peak incident fluence profiles for shots no. 6763 and 6530 in copper sheet stock.

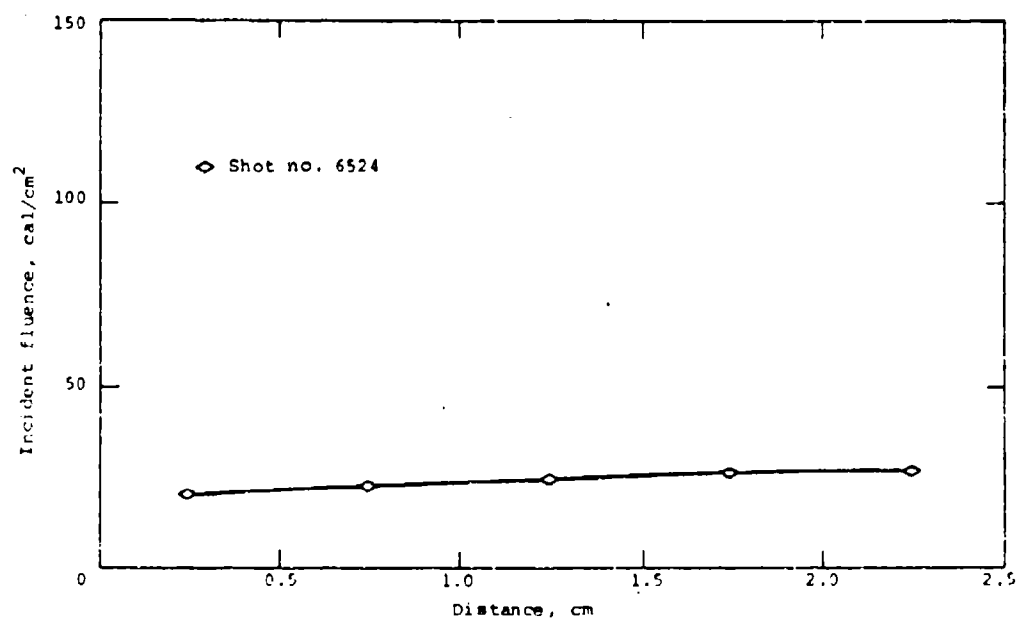


Figure C.16 Peak incident fluence profiles for shot no. 6524 in copper.

APPENDIX D

REAR SURFACE SPALL THRESHOLDS OBTAINED BY
PULSED ELECTRON BEAM TECHNIQUES

Targets of 6061-T6 aluminum just thicker than the range of $<1 \text{ MeV}>$ electrons were irradiated at fluence levels sufficient to cause rear surface spall without any accompanying front surface damage. The incident fluence was estimated from calorimeters surrounding the targets. Standard thin foil aluminum depth-dosimeters were used to estimate the time-integrated deposition profiles shown in Figure D-1.

The results of the spall tests are summarized in Table D-1. The typical appearance of a rear surface spall is shown in Figure D-2.

The above noted experiments were repeated with quartz gauges bonded to the rear surface of the samples at fluence levels bracketting the spall thresholds. Due to the absence of front surface effects, the time history of the compressive portion of the thermomechanical stress wave permits a relatively straight forward material response calculation of the stress history at the spall plane. In addition, the heated region for $<1 \text{ MeV}>$ electrons in aluminum is acoustically thick and therefore the quartz gauge data can also be used to determine the pressure-energy coupling coefficient.

These results are summarized in Table D-2. Experimental quartz gauge records are shown in Figure D-3. The time-dependence of deposition was estimated by matching an averaged experimental profile with a Spencer's data calculation using a typical accelerator current trace (Figure D-4). The time dependence is shown in Figure D-5 and summarized in Table D-3.

The measured stresses in quartz agree well with those predicted by POD, our 1-D Lagrangian code. Figures D-6 and D-7 show examples of measured and predicted stress wave profiles. Lundergan's data for 6061-T6, a Von Mises yield model, and other parameters given in Table D-5 were used in the calculations.

The deduced pressure-energy relation is shown in Figure D-8. The resulting Gruneisen parameter is $\Gamma \approx 2.0$.

Incipient spall, as shown by the photomicrograph in Figure D-2, occurs at a tensile stress of approximately 13.25 kbar which is in agreement with the measurements of General Motors and Effects Technology, Inc. for comparable tensile pulse lengths ($\sim 0.3 \mu\text{sec}$). The location of the spall is shown in Figure D-9, superimposed on a calculated (POD) peak tension envelope for the shot in question.

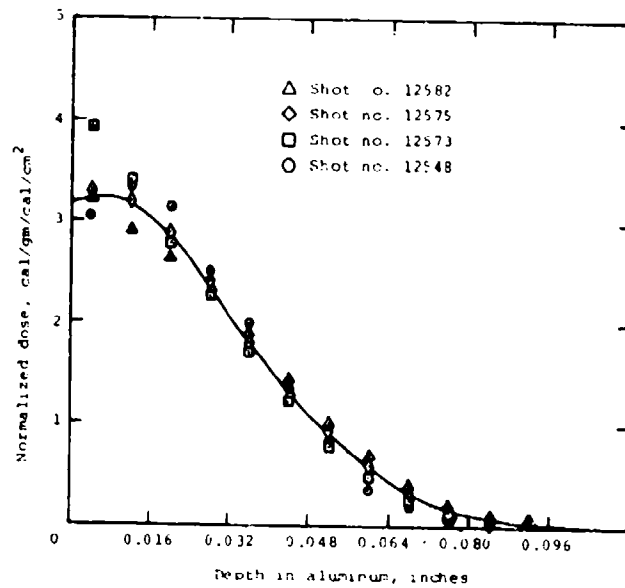


Figure D.1 Time integrated (experimental) deposition profile in 6061-T6 aluminum for <1 MeV> electrons.

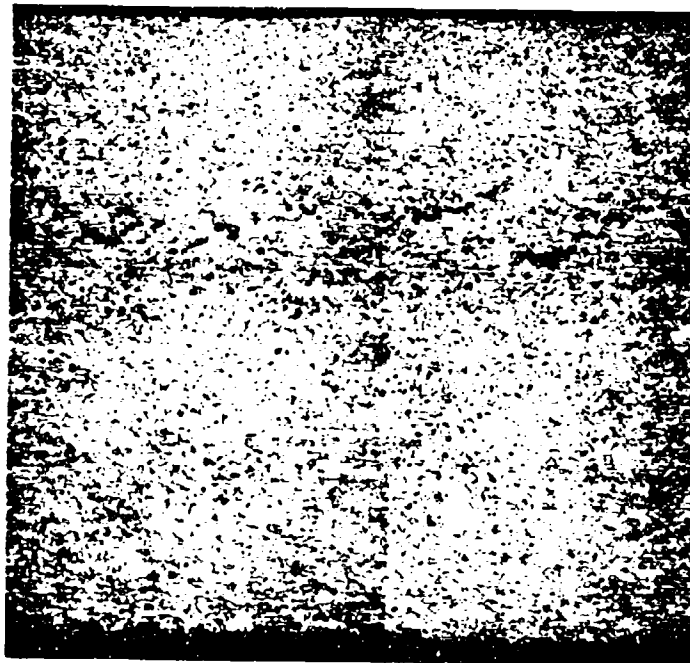
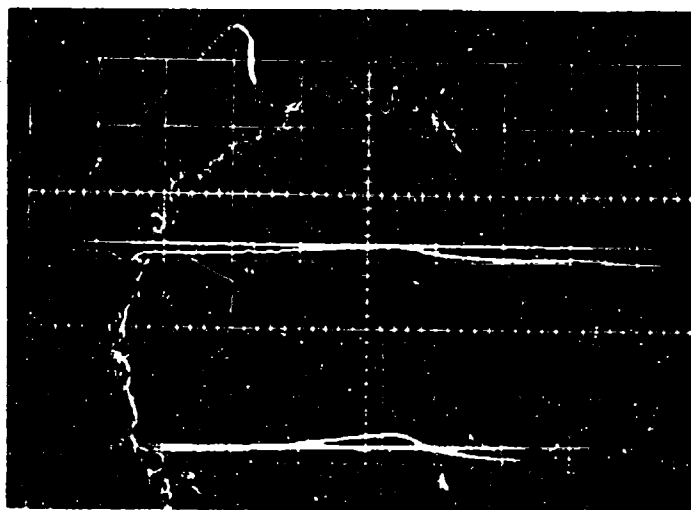
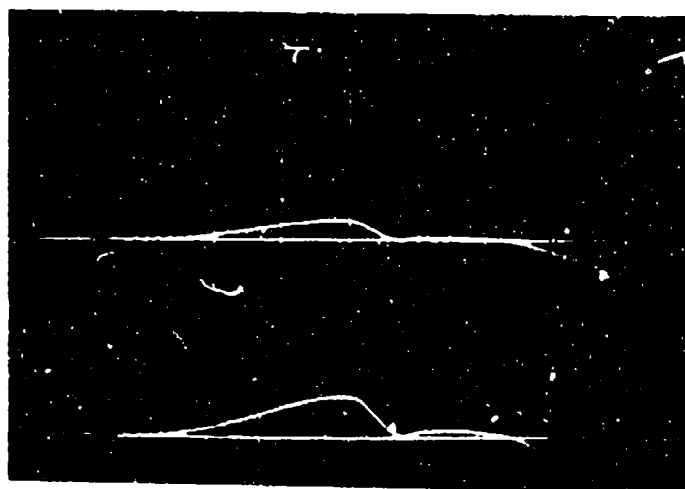


Figure D.2 Metallography of rear surface spall for shot no. 12570 in 6061-T6 aluminum (magnified 50X, target thickness = 0.098 inch).

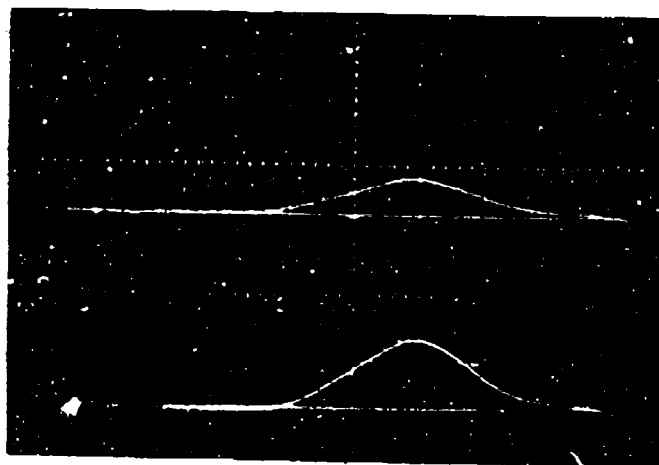


(a) Shot no. 12588

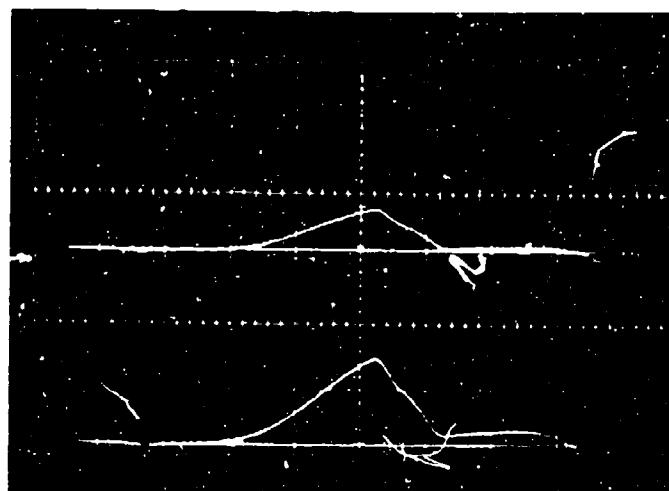


(b) Shot no. 12579

Figure D.3 Pressure response of a quartz gauge to deposition of electron energy in a thick 6061-T6 aluminum target (time scale: 0.10 $\mu\text{sec/cm}$; pressure scale: upper trace 20 V/cm, lower trace 10 V/cm; conversion factor 2.07 V/kbar).

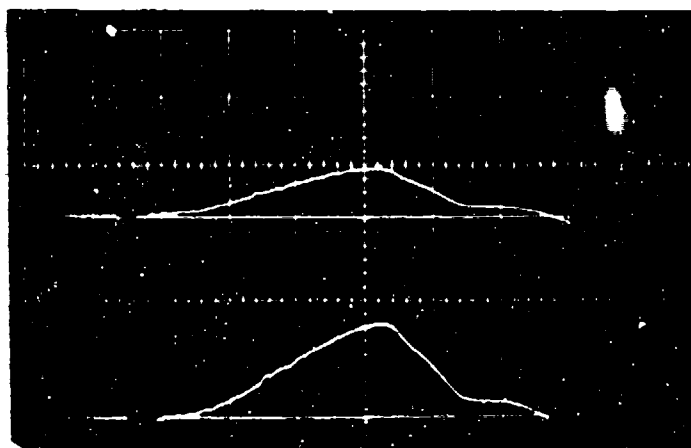


(c) Shot no. 12589

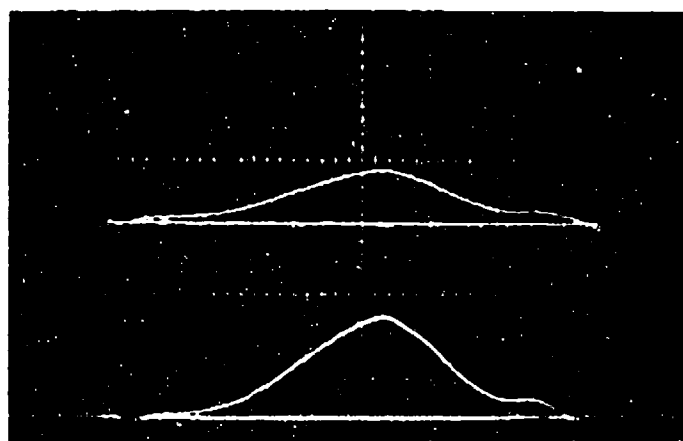


(d) Shot no. 12580

Figure D.3 (continued)

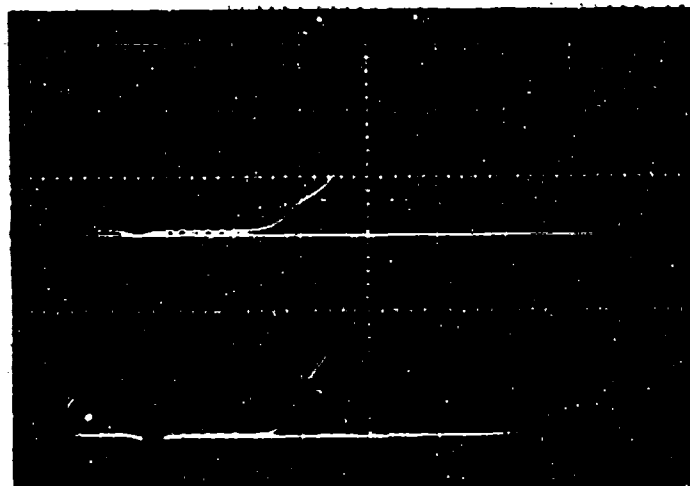


(e) Shot no. 12587



(f) Shot no. 12581

Figure D.3 (continued)



(g) Shot no. 12583

Figure D.3 (continued)

NOT REPRODUCIBLE

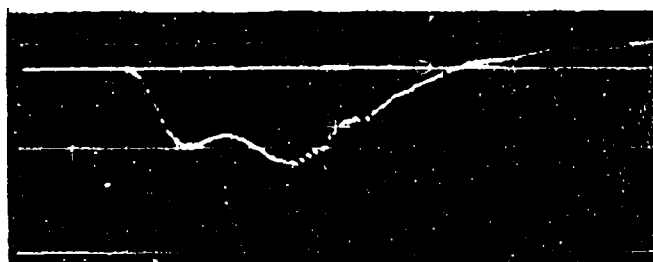


Figure D.4 Current monitor trace for shot no. 12575.

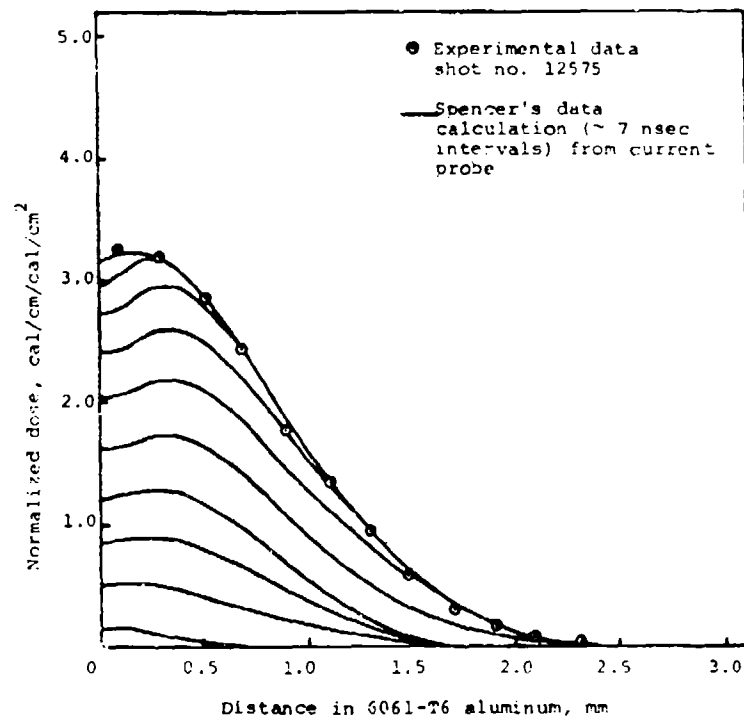


Figure D.5 Time dependent energy deposition in 6061-T6 aluminum for <MeV> electrons.

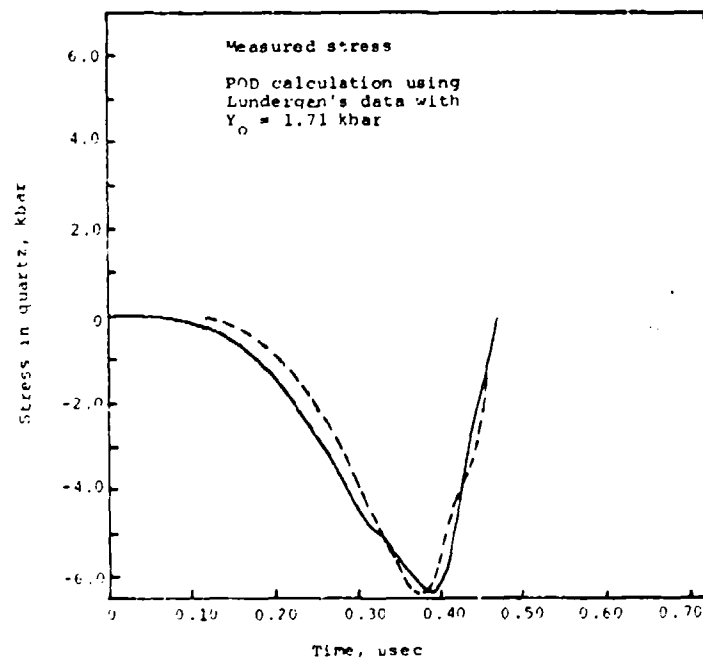


Figure D.6 Quartz gauge stress-history for shot no. 12580.

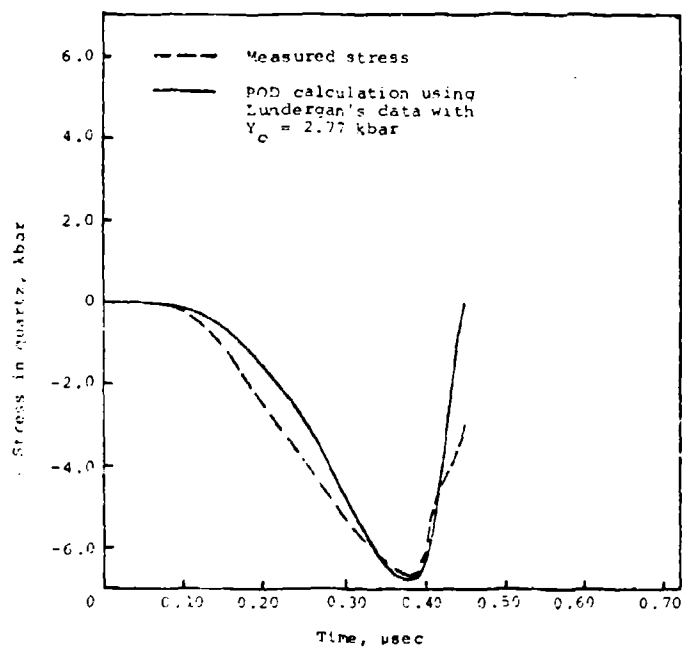


Figure D.7 Quartz gauge stress-history for shot no. 12587.

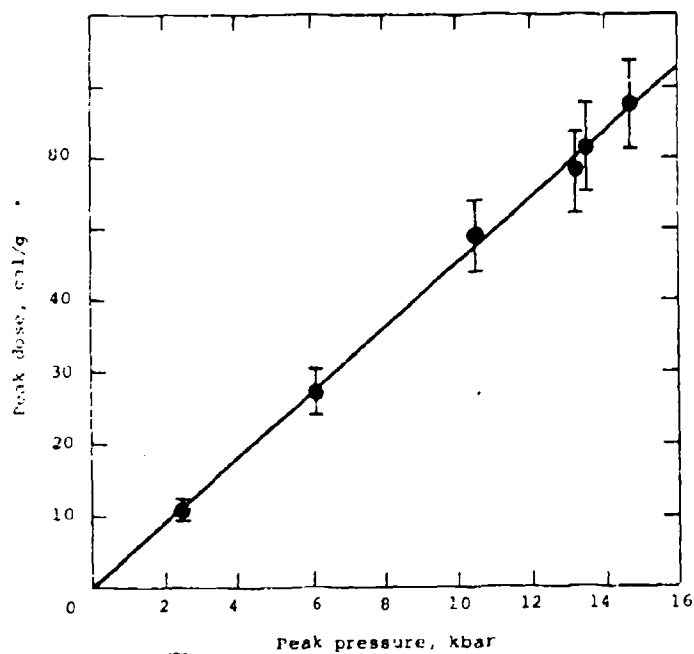


Figure D.8 Measured pressure-energy coupling in 6061-T6 aluminum.

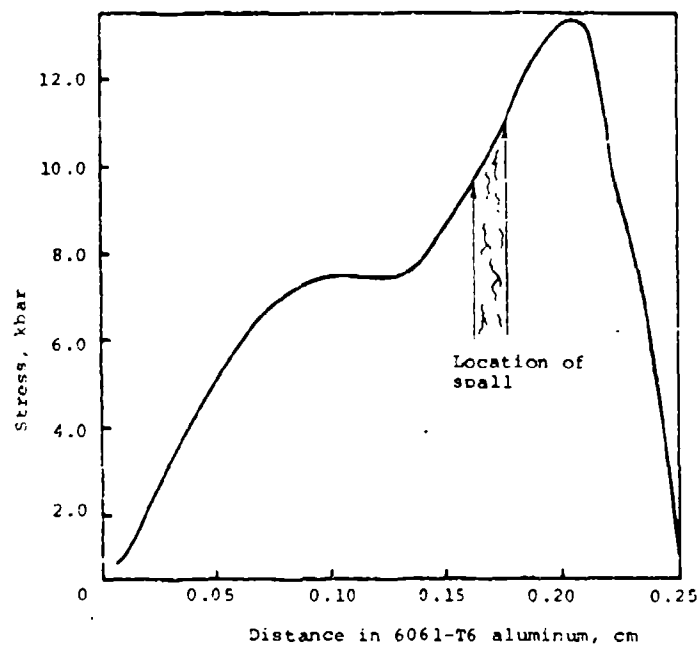


Figure D.9 Calculated peak tension envelope for shot no. 12570 and observed location of rear surface spall.

TABLE D-1
REAR SURFACE SPALL DATA FOR 6061-T6 ALUMINUM*

| Shot Number | Sample Thickness (in.) | Peak Normalized Dose [(cal/g)/(cal/cm ²)] | Average Incident Fluence (cal/cm ²) ± 10% | Average Dose (cal/g) ± 10% | Degree of Spall |
|-------------|------------------------|---|---|----------------------------|------------------------|
| 12574 | 0.100 | 0.306 | 7 | 21.4 | No Spall |
| 12552 | 0.100 | 0.306 | 11.7 | 35.8 | No Spall |
| 12553 | 0.098 | 0.306 | 12.5 | 38.3 | No Spall |
| 12572 | 0.100 | 0.306 | 13.2 | 40.4 | No Spall |
| 12549 | 0.101 | 0.306 | 15 | 45.9 | Beginning Incipient |
| 12569 | 0.099 | 0.306 | 15.8 | 48.3 | Beginning Incipient |
| 12551 | 0.099 | 0.306 | 16.4 | 50.2 | Intermediate Incipient |
| 12570 | 0.098 | 0.306 | 19 | 58.1 | Intermediate Incipient |

* <1 MeV> electrons, no front surface damage

TABLE D-2
PRESSURE-ENERGY COUPLING IN 6061-T6 ALUMINUM,
<1 MeV> ELECTRONS, QUARTZ GAUGE JUST BEYOND ELECTRON RANGE

| Shot Number | Average (±10%) Incident Fluence (cal/cm ²) | Peak Absorbed Dose* (cal/g) | Measured Peak Normal Stress in Quartz (kbar) | Predicted (POD) Peak Normal Stress in Quartz (kbar) | Predicted (POD) Peak Pressure in Aluminum (kbar) | Estimated Peak Pressure in Aluminum from Measured Normal Stress (kbar) |
|-------------|--|-----------------------------|--|---|--|--|
| 12588 | 3.5 | 10.7 | 1.22 | 1.22 | 2.44 | 2.44 |
| 12579 | 8.9 | 27.2 | 2.95 | 3.01 | 6.22 | 6.09 |
| 12589 | 16.0 | 49.0 | 5.08 | 5.42 | 11.15 | 10.48 |
| 12580 | 19.0 | 58.1 | 6.43 | 6.43 | 13.25 | 13.25 |
| 12587 | 20.0 | 61.2 | 6.60 | 6.80 | 13.90 | 13.50 |
| 12581 | 22.0 | 67.4 | 7.25 | 7.50 | 15.30 | 14.80 |
| 12593 | > 85.0 | -- | 4.0** | 4.0 | -- | -- |

* In the region where no pressure relief occurs during the deposition time

** Elastic Precursor Amplitude

TABLE D-3
 CUMULATIVE NORMALIZED DOSE [(cal/g)/(cal/cm²)] IN 6061-T6 ALUMINUM,
 <1 MeV> ELECTRONS, SPENCER'S DATA CALCULATION FOR SHOT 12575

| Distance in 6061-T6 Aluminum (mils) → | | | | | | | | |
|---------------------------------------|--------|--------|--------|--------|--------|--------|--------|--------|
| | 0 | 12 | 24 | 30 | 48 | 60 | 72 | 84 |
| 6.47 | 0.1566 | 0.0902 | 0.0127 | 0 | 0 | 0 | 0 | 0 |
| 12.94 | 0.5037 | 0.4863 | 0.3429 | 0.2015 | 0.0989 | 0.0238 | 0 | 0 |
| 19.41 | 0.8606 | 0.8922 | 0.7006 | 0.4333 | 0.1996 | 0.0358 | 0 | 0 |
| 25.89 | 1.2122 | 1.2945 | 1.0482 | 0.6500 | 0.2828 | 0.0441 | 0 | 0 |
| 32.36 | 1.6294 | 1.7362 | 1.4938 | 1.0340 | 0.5910 | 0.2702 | 0.1055 | 0.0280 |
| 38.83 | 2.0523 | 2.1811 | 1.9463 | 1.4312 | 0.9183 | 0.5247 | 0.2293 | 0.0504 |
| 45.30 | 2.4268 | 2.5981 | 2.3341 | 1.7112 | 1.0799 | 0.5700 | 0.2300 | 0.06 |
| 51.77 | 2.7344 | 2.9633 | 2.5802 | 1.9000 | 1.0900 | 0.5700 | 0.2300 | 0.06 |
| 58.24 | 2.9605 | 3.1738 | 2.6100 | 1.800 | 1.09 | 0.57 | 0.23 | 0.06 |
| 69.33 | 3.18 | 3.18 | 2.61 | 1.8 | 1.09 | 0.57 | 0.23 | 0.0600 |

TABLE D-4
 PARAMETERS USED IN THE CALCULATIONS

| Material | Gruneisen Parameter | Density (g/cm ³) | Shear Modulus (Mbar) | Yield Stress (Mbar) | $P = C_0 + \Gamma (1+\mu)E$ |
|----------|---------------------|------------------------------|----------------------|---------------------|-----------------------------|
| 6061-T6 | 2.13 | 2.70 | 0.1875 | 0.00171 | $C = 0.794$ |
| Quartz | 1.17 | 2.65 | 0.3765 | 0.02 | $C = 0.374$ |

DISTRIBUTION LIST

DEPARTMENT OF DEFENSE

Director
Advanced Research Projects Agency
Architect Building
1400 Wilson Boulevard
Arlington, Virginia 22209
Attn: Strategic Technology
Office

Assistant to the Secretary of
Defense
(Atomic Energy)
Washington, D. C. 20301
Attn: Document Control

Director
Defense Atomic Support Agency
Washington, D.C. 20305
Attn: DDST
Attn: SPAS
Attn: APSI (Archives)
Attn: STSP
Attn: APTL (Technical
Library) (2 copies)

Director
Defense Communications Agency
Washington, D.C. 20305
Attn: NMCSSC (Code 510)

Administrator
Defense Documentation Center
Cameron Station--Building 5
Alexandria, Virginia 22314
Attn: Document Control
(12 copies)

Director
Defense Intelligence Agency
Washington, D.C. 20301
Attn: DT-1C, Nuc. Energy
Branch, Dr. Jack
Vorona, Chief
Attn: DT-2 Weapons and
Systems Division

Director of Defense Research
and Engineering
Washington, D.C. 20301
Attn: Dep. Dir.
(Strategic and
Space Sys.), Dr.
Roland F. Herbst
Attn: Asst. Dir.
(Strategic Weapons),
Mr. Ben T. Plymale

Commander
Field Command
Defense Atomic Support Agency
Sandia Base
Albuquerque, New Mexico 87115
Attn: FCWD-C
Attn: Technical Library,
FCWS-SC

Chairman
Joint Chiefs of Staff
Washington, D.C. 20301
Attn: J-3, Operations
Attn: J-5, Plans and
Policy (R&D
Division)

Director
Joint Cont. Def. Sys. Integr.
Planning Staff
Commonwealth Building
1320 Wilson Boulevard
Arlington, Virginia 22209
Attn: Applied Sciences
Division
Attn: Weapon Systems
Division

Director
Joint Strategic Target Planning
Staff
Offutt AFB
Omaha, Nebraska 68113
Attn: JLTW
Attn: JPTP

Chief
Las Vegas Liason Office
Test Command, DASA
P.O. Box 2702
Las Vegas, Nevada 89104
Attn: Document Control

Chief
Livermore Division, Field Command
DASA
Lawrence Radiation Laboratory
P.O. Box 808
Livermore, California 94550
Attn: FCWD-D

Commander
Test Command
Defense Atomic Support Agency
Sandia Base
Albuquerque, New Mexico 87115
Attn: Document Control

Director
Weapons Systems Evaluation Group,
UDDR&E
Office, Secretary of Defense
400 Army-Navy Drive
Washington, D.C. 20305
Attn: Capt. Donald E.
McCoy, USN

DEPARTMENT OF THE ARMY

Director
Advanced Ballistic Missile
Defense Agency
Commonwealth Building
1320 Wilson Boulevard
Arlington, Virginia 22209
Attn: CRDABM-DD, Mr. Archie
Gold
Attn: CRDABM-NE, Ltc. James
H. Sloan

Chief
Army Nuclear Effects Laboratory
Edgewood Arsenal, Maryland 21010
Attn: AMXRD-BNL, Technical
Library

Assistant Chief of Staff for
Force Development
Department of the Army
Washington, D.C. 20310
Attn: Director of
Chemical and
Nuclear Operations

Director
Ballistic Research Laboratories
Aberdeen Proving Ground,
Maryland 21005
Attn: AMXBR-TB
Attn: Mr. Gerald L. Moss
Attn: AMXRD-BVL, Dr.
William J. Schuman

Chief of Research and
Development
Department of the Army
Washington, D.C. 20310
Attn: NCB Division,
Ltc. C. R. Sykes

Department of the Army
Harry Diamond Laboratories
Washington, D.C. 20438
Attn: AMXDO-NP
Attn: AMXDO-RBH, Mr.
Paul A. Caldwell,
Jr., R&D Supervisor

Commanding Officer
Picatinny Arsenal
Dover, New Jersey 07801
Attn: SMUPA-TN, Mr.
Burton V. Franks,
Nuclear Eng. Div.
Attn: SMUPA-VP, Dr. Don
Miller, Materials
Eng. Lab.
Attn: SMUPA-VC, Mr.
Murray Weinstein,
Eng. Sciences Lab.

Commanding General
Safeguard System Command
P.O. Box 1500
Huntsville, Alabama 35807

Attn: SSC-DRS, Mr. J. Glenn
Buxbaum

Attn: SSC-DN, Maj. Charles
C. Muses

Attn: SSC-DH, Col. Robert
A. Purple

Attn: SSC-DH, Mr. Henry L.
Solomonson

Commanding Officer
Safeguard System Evaluation
Agency

White Sands Missile Range,
New Mexico 88002

Attn: SAFSEA-E

Safeguard System Manager
Safeguard System Office
1320 Wilson Boulevard
Arlington, Virginia 22209

Attn: CSSSO

Attn: John Shea

Director

U. S. Army Advanced Ballistic
Missile Defense Agency

Huntsville Office

P.O. Box 1500

Huntsville, Alabama 35807

Attn: CRDABH-S, Mr. William
C. Loomis

Attn: CRDABH-X, Mr. Julian
Davidson

Attn: CRDABH-S, Mr. Melvin
T. Capps

Commanding Officer
U. S. Army Combat Developments
Command

Combat Support Group
Fort Belvoir, Virginia 22060

Attn: CSGS-A-S

Commanding Officer
U. S. Army Combat Developments
Command

Institute of Nuclear Studies
Fort Bliss, Texas 79916

Attn: COINS-E

Commanding Officer
U. S. Army Foreign Science and
Technology Center
220 7th Street NE
Charlottesville, Virginia 22901
Attn: Research and Data
Branch

Commanding Officer
U. S. Army Materials and
Mechanics Research Center
Watertown, Massachusetts 02172
Attn: AMXMR-X, Mr. F.
Dignam

Commanding General
U. S. Army Materiel Command
Washington, D.C. 20315
Attn: AMCRD-BN-RE, Mr.
Normand Stulman
Attn: AMCRD-BN-RE-2, Mr.
John J. F. Corrigan

Commanding General
U. S. Army Missile Command
Redstone Arsenal
Huntsville, Alabama 35809
Attn: AMSMI-RR, Mr. Lloyd
L. Lively, Nuclear
Program Manager
Attn: AMCPM-PE-E, Mr.
Scott D. Cozby,
Pershing Project
Office
Attn: AMSMI-XS, Chief
Scientist

DEPARTMENT OF THE NAVY

Assistant Secretary of the Navy
(Research and Development)
Navy Department
Washington, D. C. 20350

Chief of Naval Material
Navy Department
Washington, D.C. 20360
Attn: Mat 0323, Mr. Irving
Jaffe

Chief of Naval Operations
Navy Department

Washington, D. C. 20350

Attn: OP-752D

Attn: OP-97

Attn: OP-754

Chief of Naval Research

Department of the Navy

Arlington, Virginia 22217

Attn: Code 418, Dr. Thomas
P. Quinn, Dir. Field
Projects Prog.

Commander

Naval Ordnance Laboratory

Silver Spring, Maryland 20910

Attn: Code 121, Navy
Nuclear Programs
Office

Attn: Code 230, Dr. Carl
Boyars

Attn: Code 2302, Mr. Leo F.
Gowen

Attn: Code 322, Dr. Victor
C. Dawson

Attn: Code 031, Dr. R. K.
Lobb

Director

Naval Research Laboratory

Washington, D.C. 20390

Attn: Code 5180, Mr. M. A.
Persfchino

Attn: Code 2027, Technical
Library

Attn: Code 7680, Mr.
Laverne S. Birks

Commanding Officer

Naval Weapons Evaluation Facility

Kirtland Air Force Base

Albuquerque, New Mexico 87117

Attn: Document Control

Director

Strategic Systems Project Office

Department of the Navy

Washington, D.C. 20390

Attn: SP-273, LCDR Kenneth
C. Malley, Section
Head

Attn: SP-272, CDR Robert J.
Stinner, Section Head

DEPARTMENT OF THE AIR FORCE

AF Cambridge Research

Laboratories, AFSC

L. G. Hanscom Field

Bedford, Massachusetts 01730

Attn: SUDL, AFCRL

Research Library

AF Materials Laboratory, AFSC

Wright-Patterson AFB, Ohio 45433

Attn: MANE, Mr. George
Schmidt

Attn: Dr. T. Nicholas

Attn: MAS

Attn: Dr. Allen M. Lovelace

Commander

AF Special WEapons Center, AFSC

Kirtland AFB, New Mexico 87117

Attn: SWTSX, Survivability/
Vulnerability Branch

AF Weapons Laboratory, AFSC

Kirtland AFB, New Mexico 87117

Attn: DDGL, Technical
Library

Attn: SR

Attn: SRR

Attn: CA, Maj. William A.
Whitaker

Headquarters

Air Force Systems Command

Andrews AFB

Washington, D.C. 20331

Commander

Arnold Engineering Development

Center, AFSC

Arnold Air Force Station,

Tennessee 37389

Attn: Ltc. Fletcher

Chief of Staff
U. S. Air Force
Washington, D.C. 20330
Attn: RDPM (Missile Systems
Div., Dir. of Dev. &
Acq.)
Attn: RDQ (Director of
Opnl. Req. & Dev.
Plans)
Attn: RDQPN (S/V & Nuclear
Programs Division)
Attn: RD (DCS Research &
Development)
Attn: OA
Attn: RO-SM

Commander
Foreign Technology Division, AFSC
Wright-Patterson AFB, Ohio 45433
Attn: TDPTN
Attn: TDFBD, J. D. Pumphrey

Commander
Space & Missile Systems
Organization (SAMSO)
Los Angeles, California 90045
Attn: SYS

Space and Missile Systems
Organization, AFSC
Norton AFB, California 92409
Attn: RNSE, Environmental
Technology Branch
Attn: MMV, Reentry Systems
Division
Attn: SYSN, Survivability
Program Manager
Attn: RNS, Systems
Definition Division

Commander
Strategic Air Command
Offutt AFB, Nebraska 68113
Attn: OAl
Attn: OAN
Attn: XPPS
Attn: DOXT

ATMOIC ENERGY COMMISSION

Los Alamos Scientific Laboratory
P.O. Box 1663
Los Alamos, New Mexico 87544
Attn: Document Control for
Mr. L. C. Horpedahl
Attn: Document Control for
Dr. M. J. Katz
Attn: Document Control for
Dr. W. Lyons
Attn: Document Control for
Dr. J. W. Taylor

Sandia Laboratories
Livermore Laboratory
P.O. Box 969
Livermore, California 94550
Attn: Document Control for
Mr. Larry Baaken
Attn: Document Control for
Mr. P. D. Gildea
Attn: Document Control for
Dr. T. Gold

Sandia Laboratories
P.O. Box 5800
Albuquerque, New Mexico 87115
Attn: Document Control for
Org. 5160, Dr. Walter
Herrmann
Attn: Document Control for
Org. 1224, Dr. Albert
J. Chabai
Attn: Document Control for
Dr. D. McCloskey
Attn: Document Control for
Dr. L. Tyler
Attn: Document Control for
Org. 1710, Mr.
Charles Winter
Attn: Document Control for
Org. 5235, Dr. R.
Ewing
Attn: Document Control for
Org. 100, Mr.
Waldemar A. Klikoff,
Jr.

University of California
Lawrence Radiation Laboratory
Technical Information Division
P.O. Box 808

Livermore, California 94550

Attn: Dr. C. Joseph Taylor,
L-79

Attn: Dr. R. N. Keeler,
L-504

Attn: Dr. R. Wagner, L-31

Attn: Dr. Lawrence S.
Germain, L-18

OTHER GOVERNMENT

Central Intelligence Agency
Washington, D. C. 20505

Attn: Genevieve Ashby--
RD/SI--5G48 HQS

DEPARTMENT OF DEFENSE CONTRACTORS

Aeronautical Research Associates
of Princeton, Inc.
50 Washington Road
Princeton, New Jersey 08540
Attn: President & Senior
Consultant, Dr. C. Donaldson

Aerospace Corp.
P.O. Box 5866
San Bernardino, California 92408
Attn: Dr. Richard G. Allen
Attn: Gp. Dir., Adv. Sub-
systems, Dr. Richard Hartunian
Attn: Weapons Effects Dept.,
Dr. Sidney W. Kash
Attn: Weapons Effects Dept.,
Dr. F. Arlen Field
Attn: Director, Hardened
Reentry Systems, Dr. R. Mortensen

Aerospace Corporation
P.O. Box 95085
Los Angeles, California 90045
Attn: Off. of Tech. Surviv.
Dir. (Dr. Harris Mayer)

AVCO
Government Products Group
201 Lowell Street
Wilmington, Massachusetts 01887
Attn: Mr. George J. Davis,
S320, Room 3185
Attn: Mr. John Gilmore,
E502, Room 1263
Attn: Mr. John E. Stevens,
E500, Room 1208
Attn: Mr. Thomas R. Munson,
E540, Room 1206
Attn: Dr. William Reinecke,
W230, Room 5204
Attn: Document Control,
A820, Room 1107

Battelle Memorial Institute
505 King Avenue
Columbus, Ohio 43201
Attn: R. Castle

Bell Telephone Laboratories
Mountain Avenue
Murray Hill, New Jersey 07971
Attn: Mr. M. F. Stevens
Attn: Mr. R. S. Weiner
Attn: Mr. C. A. Lapadula

Boeing Company, The
P.O. Box 3707
Seattle, Washington 98124
Attn: Mr. Jack George
Attn: B. Clingan
Attn: J. Edson

Effects Technology, Inc.
5383 Holister Avenue
Santa Barbara, Calif. 93105
Attn: Dr. Donald V.
Keller, President

EG&G, Inc.
P.O. Box 227
Bedford, Massachusetts 01730

General Electric Company
Tempo-Center for
Advanced Studies
816 State Street
Santa Barbara, Calif. 93102
Attn: DASA Information
and Analysis Center

General Electric Company
Space Division
Valley Forge Space Center
P.O. Box 8555
Philadelphia, Pa. 19101
Attn: Phillip Cline
Attn: Dr. C. Anderson
Attn: Mr. T. Bechtel
Attn: Dr. B. Walker

General Motors Corporation
Manufacturing Development
Manufacturing Staff
12 Mile and Mound Roads
Warren, Michigan 48090
Attn: Supervisor-
Physics Engineering
Mr. William M. Isbell

General Research Corporation
P.O. Box 3587
Santa Barbara, Calif. 93105
Attn: Technical Information
Office for Mr. Robert E.
Rosenthal

General Research Corporation
1501 Wilson Boulevard
Arlington, Virginia 22209
Attn: Dr. Giles F. Crimi
Attn: Dr. Earl Crisler

Gulf Oil Corporation
P.O. Box 1111
San Diego, California 92112
Attn: F. W. Simpson, Chief,
TISD for CGA

Institute for Defense Analyses
400 Army-Navy Drive
Arlington, Virginia 22202
Attn: Tech. Info. Office
Attn: Dr. Joel Rengston
Attn: Dr. J. Menkes

Kaman Avidyne
Division of Kaman Sciences Corp.
83 Second Avenue
Northwest Industrial Park
Burlington, Massachusetts 01803
Attn: General Manager,
Donald P. Hobbs

Kaman Sciences Corporation
Kaman Nuclear Division
1700 Garden of the Gods Road
Colorado Springs, Colorado 80907
Attn: Dr. F. H. Shelton
Attn: Dr. A. P. Bridges
Attn: Dr. J. R. Hoffman
Attn: Mr. Thomas F. V. Meager
Attn: Mr. J. L. Harper

KMS Industries, Inc.
KMS Technology Center
7810 Burnet Avenue
Van Nuys, California 91405
Attn: Daniel Bloxsom

Lockheed Missiles & Space Co.
Div. of Lockheed Aircraft Corp.
P.O. Box 504
Sunnyvale, California 94088
Attn: J. Massard (5220)
Attn: K. Foresberg (5220)
Attn: L. Hearne (8114)
Attn: D. M. Teller

Martin Marietta Corp.
Orlando Division
P.O. Box 5837
Orlando, Florida 32805
Attn: Eng. Dept. Staff,
Mr. H. Goldmacher, MP-413
Attn: Mr. J. M. Potts,
Senior Staff Engineer,
MP-121
Attn: Mr. W. A. Gray,
Senior Staff Engineer,
MP-61

McDonnell Douglas Corp.
3000 Ocean Park Boulevard
Santa Monica, Calif. 90406
Attn: A-253-JC54 M/S 8,
Mr. H. L. Herdman
Attn: A-253-JC54 M/S 8,
Mr. K. A. McClymonds

McDonnell Douglas Corp.
5301 Bolsa Avenue
Huntington Beach, Calif. 92647
Attn: A3-833-BBRO M/S 9,
Mr. A. W. Maddox
Attn: A3-833-BBGO M/S 9,
Dr. H. M. Berkowitz
Attn: A3-830-BBGO M/S 9,
Mr. J. F. Garibotti
Attn: A3-833-BBGO M/S 9,
Dr. R. J. Reck

National Academy of Sciences
2101 Constitution Avenue, N.W.
Washington, D.C. 20418
Attn: National Materials
Advisory Board,
Mr. Donald G. Groves

Northrop Corporation
Northrop Corporate Laboratories
3401 West Broadway
Hawthorne, California 90250
Attn: Dir., Solid State
Electronics, Dr. Orlie L.
Curtis, Jr.
Attn: Dr. D. A. Hicks
Attn: Vice President & Mgr.,
Dr. Walter E. Crandall

Philco-Ford Corporation
Aeronautronic Division
Ford & Jamboree Roads
Newport Beach, California 92663
Attn: Dr. L. K. Goodwin
Attn: J. Shea

Physics International Company
2700 Merced Street
San Leandro, California 94577
Attn: Document Control for
Mr. Alan Klein, Department
Manager

R&D Associates
P. O. Box 3580
Santa Monica, California
Attn: Dr. Albert L. Latter

Science Applications, Inc.
P.O. Box 2351
La Jolla, California 92037
Attn: Dr. William M. Layson

Southwest Research Institute
8500 Culebra Road
San Antonio, Texas 78228
Attn: Mgr., Engineering
Dynamics Section
Dr. Wilfred E. Baker

Stanford Research Institute
4810 Bradford Blvd., N.W.
Huntsville, Alabama 35805
Attn: Senior Nuclear Engineer
Mr. Harold R. Carey

Stanford Research Institute
333 Ravenswood Avenue
Menlo Park, California 94025
Attn: Dr. G. R. Abrahamson
Attn: Dr. R. C. Crewdson
Attn: Dr. E. M. Kinderman
Attn: Dr. H. E. Lindberg

Systems, Science & Software, Inc.
P.O. Box 1620
La Jolla, California 92037
Attn: Dr. R. A. Kruger
Attn: Dr. R. E. Duff

TRW Systems Group
One Space Park
Redondo Beach, California 90278
Attn: Dr. C. Stowe
Attn: Dr. C. Busch
Attn: Dr. J. I. Slaughter
Attn: Dr. B. Sussholtz

TRW Systems Group
San Bernardino Operations
P.O. Box 1310
San Bernardino, Calif. 92402
Attn: Dr. E. W. Allen
Senior Staff Scientist
Attn: L. Berger